Assessing Predictive Accuracy of Tornado Resilience Models Through Post-Event Reconnaissance Data Analysis

Preprint Notice

This manuscript is a preprint and has not undergone peer review. It has been submitted for consideration for publication in an academic journal. The content presented herein may be revised, supplemented, or modified following the peer-review process.

Corresponding author:
Pramodit Adhikari
Department of Civil and Environmental Engineering
University of Nebraska–Lincoln
Email: adhikaripramodit@huskers.unl.edu

Assessing Predictive Accuracy of Tornado Resilience Models Through Post-event Reconnaissance Data Analysis

Pramodit Adhikari[1], Milad Roohi[1*], Richard L. Wood[2], and David Roueche[3]

[1]Durham School of Architectural Engineering and Construction, University of Nebraska–Lincoln.
*Email: milad.roohi@unl.edu

[2]Civil and Environmental Engineering, University of Nebraska–Lincoln

[3]Civil and Environmental Engineering, Auburn University

ABSTRACT

Community resilience assessment under a given hazard scenario is commonly performed by representing the building inventory through archetypes and assigning fragility functions for multiple limit states to each archetype. However, because these archetypes and fragility functions may be developed from design provisions, mechanics-based analyses, expert judgment, or historical event data, their transferability to other risk contexts remains uncertain, and the errors introduced by such generalization are not yet well understood. This paper presents a framework for quantifying modeling error and evaluating the transferability limitations of archetype-based fragility models when applied beyond their original risk contexts. The framework integrates exposure data, hazard characterization, fragility-based damage analysis, post-event reconnaissance observations, and risk quantification to compare predicted and observed damage states. The framework is demonstrated across five tornado-affected communities from three tornado events, exposure conditions, and community contexts. Model performance is assessed at both community and building scales by characterizing discrepancies between field observations and model predictions. Statistical associations within the examined testbed conditions are evaluated to assess how effectively the models reproduce observed damage patterns. The resulting community testbeds provide quantitative evidence regarding modeling error, uncertainty, and transferability limitations under the examined

event conditions, while supporting greater consistency between post-event reconnaissance and community model development. The findings demonstrate that current fragility frameworks, in their existing form and without systematic multi-event calibration, are not yet ready for generalized operational prediction and deployment across heterogeneous tornado environments.

Keywords: Community Resilience; Tornado Damage Assessment; Field Reconnaissance; Uncertainty Quantification; Model Transferability

INTRODUCTION

Community resilience assessment under natural hazards commonly relies on archetype-based representations of the built environment, where fragility functions are assigned to building classes to estimate physical damage, losses, and recovery outcomes (Crowley et al. 2004; Schneider and Schauer 2006; Padgett and DesRoches 2007; Cimellaro et al. 2010; Cimellaro et al. 2016; Bai et al. 2013; Gardoni 2018; Memari et al. 2018). Such approaches have been widely applied to earthquakes, hurricanes, tornadoes, and other hazards because they enable regional- and community-scale analyses while maintaining computational tractability (Hill and Levitan 2005; Vickery et al. 2006a; Kameshwar and Padgett 2014; Pita et al. 2015; Gidaris et al. 2017; Nofal et al. 2021; Ghasemi et al. 2026). Scientific and practical gaps remain in validated assessment tools, recovery-cost estimation, resilience metrics, multi-hazard criteria, system-level performance standards, and planning guidance for communities (McAllister 2018; Roohi et al. 2020).

Currently, the transferability of risk and resilience models remains insufficiently understood. In particular, the archetypes and fragility functions underlying these assessments may be developed from design provisions, mechanics-based analyses, experimental studies, expert judgment, or observations of historical events (Rossetto et al. 2013; Silva et al. 2019; Porter et al. 2007). Their applicability to communities, exposure conditions, and hazard events beyond their original development or validation contexts requires further investigation (Saeednejad and Padgett 2026; Kalakonas et al. 2020). This investigation will enhance our understanding of limitations, discrepancies between model predictions and real-world impacts, and uncertainty quantification. Ultimately, it will establish a systematic workflow for resilience assessment, particularly for natural hazards that have been historically underinvestigated.

Tornadoes represent a particularly challenging hazard for community-level risk and resilience assessment due to their highly localized, transient, and spatially variable nature. In the United States alone, approximately 1,200 tornadoes occur annually, causing substantial physical, social, and economic losses, including casualties and billions of dollars in damage (NCEI 2025; NOAA 2024). These impacts have motivated extensive research on probabilistic tornado hazard characterization (Standohar-Alfano and van de Lindt 2015), tornado fragility development (Roueche et al. 2017; Memari et al. 2018), community-level damage and resilience modeling (Attary et al. 2018; Wang et al. 2021; Adhikari et al. 2021), and post-event recovery assessment (Pilkington et al. 2021; Aghababaei et al. 2020a). Collectively, these efforts have advanced the ability to estimate tornado-induced consequences and support risk-informed decision-making at the community scale.

The Enhanced Fujita (EF) scale provides a primary framework for characterizing tornado intensity based on observed damage to 28 damage indicators and associated degrees of damage (McDonald and Mehta 2006), although direct in-situ wind measurements and remote-sensing observations are also used where available. Because direct measurements of near-surface tornado wind fields are limited, post-event damage observations serve as a critical source of information for estimating tornado intensity and understanding hazard impacts. Consequently, damage assessments play a central role in both operational tornado characterization and the development of vulnerability and fragility models used in community-level risk analyses.

To support post-event damage assessment, numerous reconnaissance and remote-sensing techniques have been developed to document and quantify tornado-induced damage. These include satellite and Uncrewed Aerial System (UAS) imagery (Myint et al. 2008; Chen et al. 2021; Brown 2010), LiDAR and photogrammetric techniques (Wakimoto et al. 2011), forensic damage investigations (Graettinger et al. 2012), tree-fall analysis (Nasimi and Wood 2024), and coordinated reconnaissance efforts such as those conducted through Structural Extreme Events Reconnaissance (StEER) (Kijewski-Correa et al. 2021; Roueche et al. 2024a; Wood et al. 2024). These datasets provide increasingly detailed observations of building performance and community impacts following tornado events. However, due to the localized and short-lived nature of tornadoes, the perishable nature of post-event evidence, and the limited availability of high-resolution observations during the event itself, accurately reconstructing tornado hazards and their consequences remains challenging. As a result, many tornado risk assessment frameworks rely on reverse-engineering approaches that infer hazard characteristics from observed damage patterns and reconnaissance data.

Several virtual and real-world testbeds have been developed to implement, verify, and improve community resilience models under natural hazards (Ellingwood et al. 2016; Attary et al. 2018; Aghababaei et al. 2020b; Wang and van de Lindt 2021b; Roueche et al. 2024b; Roohi et al. 2020; Roohi et al. 2024). Among these, the 2011 Joplin EF5 tornado has become one of the most extensively studied community-scale testbeds. Through detailed investigations conducted by the National Institute of Standards and Technology (NIST), during which they gathered extensive data, developed a model of the tornado windfield, and subsequent research efforts, comprehensive datasets describing tornado hazards, building performance, infrastructure disruptions, emergency response, and recovery processes were assembled (Kuligowski et al. 2014). These datasets enabled the development and validation of community resilience frameworks that have subsequently been adopted in numerous community-scale assessments (Attary et al. 2018; Wang et al. 2021; Pilkington et al. 2021). The fragility functions used in these frameworks, however, should not be interpreted as event-fitted empirical fragilities from the Joplin tornado record. Rather, the 19 archetype-based fragilities implemented in the Interdependent Networked Community Resilience Modeling Environment (IN-CORE) are synthesized from mechanics-based component-to-system analyses, design provisions, and ASCE 7 standard-informed structural assumptions (Wang and van de Lindt 2021b; Wang and van de Lindt 2022; Memari et al. 2018). In particular, many community-level tornado resilience studies continue to rely on the these fragility relationships, despite limited evidence of their applicability to other tornado environments and community contexts.

While many resilience metrics and community-level outcomes have been evaluated using the Joplin testbed, the transferability of the underlying fragility models to other communities and tornado events remains largely unexplored. In particular, prior IN-CORE applications report favorable performance for Joplin: Attary et al. (Attary et al. 2018) conclude that hindcasting the 2011 Joplin tornado shows "very good correlation with observed damage" at the aggregate community scale, and Wang and van de Lindt (Wang and van de Lindt 2021b; Wang et al. 2021; Wang and van de Lindt 2021a) report that damage, functionality, and recovery outcomes derived from the Joplin testbed are close to field investigation data. By contrast, the present study finds through a more granular, multi-event evaluation that the associated mechanics/code-based fragility functions do not consistently maintain predictive accuracy or transferability when applied to other community contexts or at the individual building scale. Furthermore, agreement between model predictions and observations at the community scale does not necessarily imply predictive accuracy at the individual building scale. Differences in building practices, code requirements, construction materials, socioeconomic conditions, recovery resources, urban development patterns, and hazard characteristics may all influence the applicability of fragility models outside their original development and validation context. Consequently, questions remain about whether tornado damage models developed and evaluated on a limited set of historical events can reliably predict damage across heterogeneous communities, and whether validation at the community scale translates into predictive capability at the asset scale.

To address these questions, this paper presents a framework for quantifying modeling error in community-level tornado damage assessment by integrating post-event reconnaissance observations with fragility-based damage modeling. The framework does not assume that existing fragility models are broadly generalizable; rather, it uses their application to multiple tornado-affected communities as a test case to evaluate discrepancies between predicted and observed damage. By combining exposure information, tornado hazard characterization, fragility-based damage analysis, and empirical damage observations, the framework assesses model performance at both individual-building and community scales across five communities. This work extends prior aggregate-scale validations in two respects. First, it refines the validation standard, whereas earlier IN-CORE studies established correlation at the community scale, a step that Attary et al. (Attary et al. 2018) show requires high spatial resolution, we evaluate predictive accuracy at the individual building scale and demonstrate that aggregate agreement can mask substantial discrepancies in individual predictions. Second, rather than treating the fragility functions as fixed inputs, as in studies that employ the 19 archetypes(Memari et al. 2018), we examine the foundational fragility functions themselves and show that their construction assumptions, including inadequate dispersion constraints and the potential for limit-state crossover, are direct contributors to predictive error at the asset scale. The resulting testbeds provide quantitative evidence on modeling error, uncertainty, and transferability limitations under the examined event conditions, while identifying opportunities to improve future community resilience assessments.

The paper is organized as follows: first, it introduces community-level tornado resilience analysis, focusing on the role of open-access exposure and hazard datasets in damage quantification. This is followed by a detailed introduction to the proposed methodology. Next, a section demonstrates the implications of the proposed method using community resilience models and field investigation data collected by StEER in the aftermath of three tornado events spanning five affected communities (Davidson, Wilson, and Putnam Counties from the Nashville–Cookeville event; St. Bernard Parish from the Arabi event; and Dallas County from the Dallas event). The paper subsequently presents an in-depth examination of these case studies, together with the extensively studied 2011 Joplin testbed as a baseline, and concludes with insights learned from real-world validation.

COMMUNITY-LEVEL TORNADO RESILIENCE ANALYSIS: THE ROLE OF OPEN-ACCESS EXPOSURE AND HAZARD DATASETS IN DAMAGE QUANTIFICATION

Uncertainties in community-level tornado resilience analysis arise from various components of the modeling framework, including hazard characterization, exposure assessment, vulnerability analysis, and recovery dynamics. These components introduce inherent complexities due to the stochastic nature of tornado events, variability in structural and social vulnerabilities, and limitations in available data and modeling techniques. These uncertainties can be characterized as two fundamental types: aleatory and epistemic. Epistemic uncertainties arise from a lack of knowledge. These include inaccuracies in wind load calculations due to a lack of data on building materials, configurations, aerodynamic properties, and the behavior of components or building systems. They can be minimized with additional knowledge as supplementary data becomes available to refine the model. On the other hand, aleatory uncertainties are the inherent randomness or variability in those elements that cannot be improved even with new data. The uncertainties can be reduced by improving our understanding of windfield characteristics and properties.

The uncertainties in quantifying the wind hazard and associated damage include intensity measure estimates, damage classifications, finite-sample data from a population of damaged datasets, and fragility fitting. These uncertainties associated with tornado hazard intensity and demands at both the component- and system-level introduce an additional layer of complexity to resilience analysis. This will result in either underestimation or overestimation of tornado hazard, cascading those errors into inaccurate damage predictions, which could lead to misinformation in decision-making for developing effective mitigation and recovery strategies. The paper focuses on damage prediction subsets within the larger resilience modeling framework. Fig. 1 presents the model elements that embody these uncertainties and the relationship that drives the analysis.

Open-access data, including exposure datasets, geospatial information, and hazard characteristics, supports detailed risk assessments by enabling modelers to assess the accuracy and completeness of data for future predictions. The integration of open-access data with open-source GIS tools and libraries can facilitate spatial analyses of tornado impacts within a community, thereby improving the reliability of hazard and exposure mapping. Community-level building inventories are available from various non-proprietary datasets.

Open-access data sources for building inventory development include the National Structures Inventory (NSI) (NSI 2022), Google Earth, OpenStreetMap (OSM), Bing Maps from Microsoft, and county-level Tax Assessor databases. Tornado hazard data are available from the National Weather Service (NWS) Damage Assessment Toolbox (DAT), the NWS Storm Prediction Center (SPC), and the Iowa State University (ISU) mesonet. Fragility functions for low-rise wood-framed structures exposed to wind loads are accessible from various analytical models (Rosowsky and Ellingwood 2002; Ellingwood et al. 2004). There have been efforts to develop empirical fragility functions for residential structures under tornado-induced and straight-line wind loads (Roueche et al. 2017; Cremen and Baker 2019), which could result in higher-fidelity loss predictions than the damage observed in past events. Roueche et al. (Roueche et al. 2018) evaluated the uncertainties associated with intensity measure, damage measure classification, finite sampling, fitting fragility functions, and a combination of these and identified intensity measure uncertainties to be the most significant contributor to developing empirical fragility functions. Tornado damage analysis incorporates these uncertainties to a reasonable extent through uncertainty quantification within fragility and hazard modeling.

In the following section, the authors present a generalized methodology for achieving consistent, comparable results across various scales and community testbeds by incorporating open-access datasets, accounting for sparse or inaccurate data, and using post-event reconnaissance data to identify limitations and opportunities for future refinements.

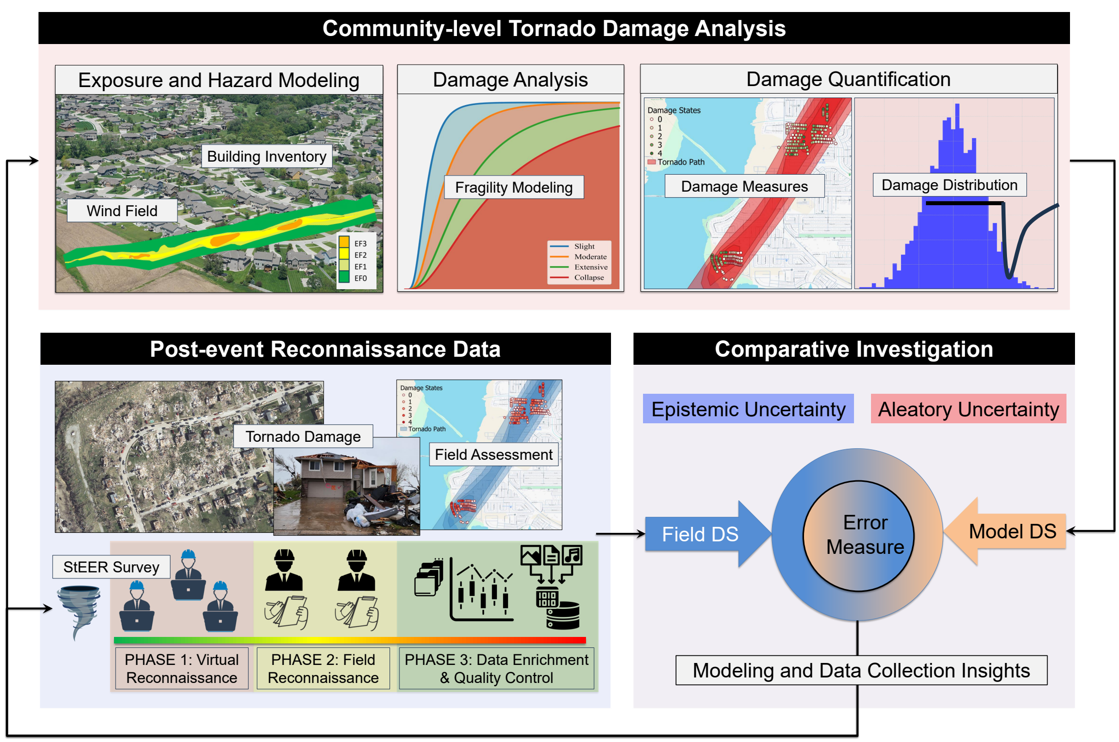

Fig. 1. The components integrating community-level damage modeling with post-event reconnaissance records for V&V of tornado damage model outcomes and evaluating the sources of uncertainty.

PROPOSED METHODOLOGICAL APPROACH

This section proposes a method to investigate current generalization and transferability limitations of the prior fragility framework by utilizing publicly accessible datasets and open-source computational modeling, and demonstrates its implementation through diverse testbed communities. The aim is to juxtapose the building damage classification from the reconnaissance $k \in 1, ..., n$ after implementing the state-of-the-art community resilience models to evaluate their predictive accuracy. A general methodology is developed for conducting a community-level tornado damage analysis and quantitative validation using the outcomes from computational modeling and reconnaissance surveys. Fig. 2 presents an overview of the proposed multi-stage methodology, which begins with the community and the tornado event and damage abstraction. This abstraction involves conceptual simplification of the real-world community structures, tornado characteristics, and damage mechanisms into model representations that capture the essential patterns and outcomes. This enables computational models to efficiently evaluate potential or actual damage across a community, especially when combined with geospatial data, fragility functions, and building archetypes. This is followed by a sequence of three general steps, including 1) reconnaissance process, 2) open-access data and modeling process, and 3) computational model development and validation. In each stage, the computational model provides damage outcomes for a community $k \in 1, ..., n$ after the implementation of the computational community models, juxtaposed with field outcomes from data collection records and findings. The outcomes are analyzed to quantify discrepancies, identify areas where model predictions deviate from empirical data, validate the model, determine the factors that influence model predictions, and suggest improvements to improve prediction frameworks. In particular, statistical measures are recorded to support an iterative learning loop in which, as more events occur and diverse community contexts and tornado intensities are encountered, the community models' reliability and transferability are characterized using statistical performance measures and newly collected data. The process workflow depicted in Fig. 2 refers to an ongoing, cross-event process in which each newly surveyed community is processed through the same three stages and contributes additional evidence on model performance; it does not denote a within-study optimization in which the fragility functions were calibrated against the field data before reporting the results. The models, archetypes, and fragility parameters used in this paper are applied as available, without community-specific parameter updating, so that the reported discrepancies reflect the as-is transferability of the existing framework rather than the performance of a model that has been adjusted to the test communities. The systematic field-informed updating that this learning loop would enable is identified as future work and could be leveraged to enhance the predictive accuracy and generalizability of tornado risk and resilience models, which is beyond the scope of this paper. The following discusses the three phases of the proposed methodology in detail.

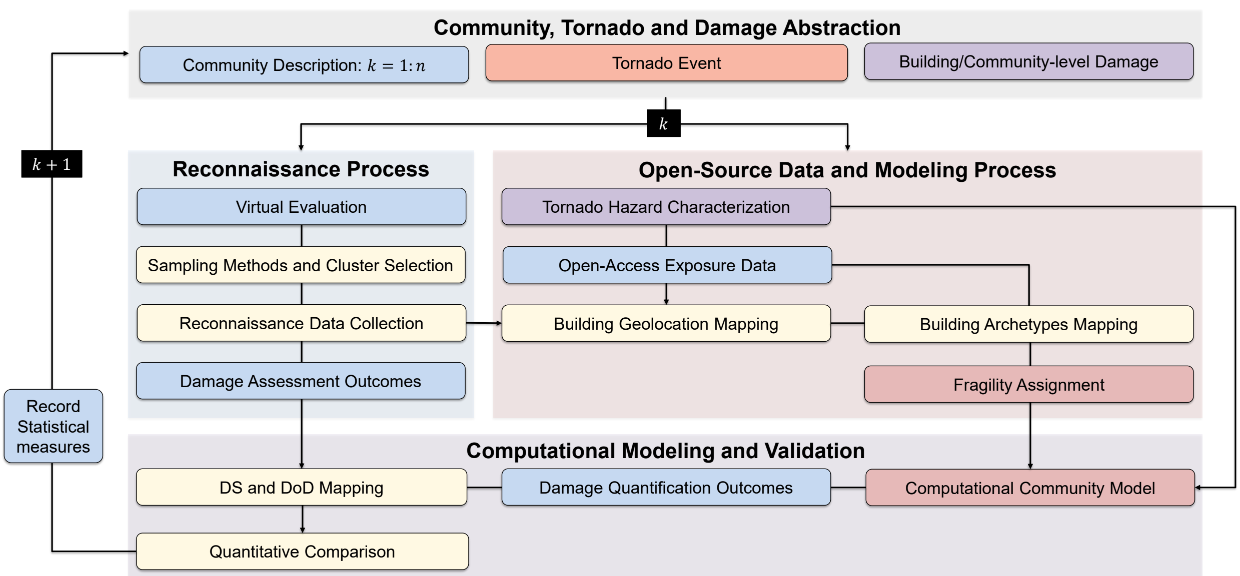

Fig. 2. The proposed methodological approach for multi-community evaluation for the transferability of a generalized community-level tornado damage assessment methodology utilizing publicly accessible datasets and open-source computational modeling.

3.1 Reconnaissance Process

Following a tornado event, the first stage consists of a reconnaissance process that includes virtual evaluation, development of sampling methods, field data collection, and damage assessment. A structured reconnaissance process is initiated to assess the extent and nature of the damage, using virtual evaluation tools such as satellite imagery and drone footage, which are often employed in the initial stages to remotely identify affected areas and prioritize ground investigations. Sampling methods and cluster selection strategies ensure representative coverage, enabling efficient allocation of survey resources across varied impact areas. During reconnaissance data collection, a field damage assessment is conducted where Degree of Damage (DoD) and Damage State (DS) are classified for several Damage Indicators (DIs). These damages are associated with the wind speeds believed to have caused the corresponding level of damage. Associating these wind speeds with the damage profiles provides the tornado wind speeds and EF-scale ratings, aiding in constructing EF-contours. The highest level of observed damage determines the EF-scale assignment for the tornado, and the contours are mapped based on the spatial distribution of the observed damage and its severity. Direct field studies and evaluations of wind damage, correlated with radar data, provide approximate predictions of tornado contours and damage swaths. However, the rapidity of the damage assessment yields low-resolution data, which limits the ability to capture the ground truths accurately. Meteorological agencies (such as the NWS in the US) conduct rapid surveys with meteorologists and damage assessment teams deployed to affected areas to inspect and evaluate the type and extent of wind damage to infrastructure and the natural environment. These field assessments are correlated and validated with the radar data, helping to reconstruct the tornado touchdown, take-off, trajectory, and intensity fields. This is done rapidly to obtain the EF scale for the tornado and its contours at different scales. The windfield typically does not align with a comprehensive field study and data collection (as demonstrated later in Section 5). The resulting damage assessments improve the classification of damage severity and strengthen the validation of computational resilience models. They also enable comprehensive quantification of community-wide impacts, supporting evidence-based recovery planning and targeted mitigation strategies.

3.2 Open-Source Data and Modeling Process

The second stage comprises an open-access data and modeling process that characterizes tornado hazards, utilizes open-access exposure data, and maps building locations and archetypes, leading to fragility assignment. The following subsections elaborate on each step.

3.2.1 *Tornado Hazard Characterization*

Tornadoes present exceptional challenges for physics-based mathematical simulation due to their complex, nonlinear dynamics and rapidly changing behavior. However, there have been efforts to simplify the tornado windfield. The gradient method of tornado simulation, as suggested by Standohar-Alfano and van de Lindt (Standohar-Alfano and van de Lindt 2015) and implemented by Masoomi and van de Lindt (Masoomi and van de Lindt 2017), has been utilized to simulate restoration and functionality of a model community in many different studies as well as implemented in various platforms for tornado hazard modeling. These methods of tornado windfield idealization are defined by gradients that represent a change in velocity or pressure with distance from the tornado center. This method enables straightforward tornado velocity estimation from building profiles and damage estimates based on wind speeds. However, wind intensity is a variable within the storm that results in stochastic interactions with the natural and built environments. There is both transverse (across the width) and longitudinal (along the length) spatial variability in the intensity along the tornado path. For a simplified model, it is assumed that in the transverse direction, the highest wind speeds occur at the tornado's center and gradually diminish outward, indicating the tornado's radial structure. Along its length, the tornado's intensity undergoes cycles or pulses, intensifying and weakening over its lifetime.

Careful consideration must be given to the setup of the tornado hazard layer. Two different approaches can be used to formulate tornado profile contours: 1) overlay different contours above each other, or 2) create a discretized set of layers for each EF-scale to combine and obtain a full tornado profile. For a simplified windfield, both are depicted at the top of Fig. 3 for an EF2 tornado. The choice between these two profile constructions yields varied and pronounced differences in the model's damage analysis. The deaggregated profile assigns each building a single intensity corresponding to its actual position within the band structure and produces results more consistent with observed field damage. The deaggregated profile is therefore adopted in this study and should be carefully considered when representing tornado hazards for damage analysis. An accurate representation of tornado profiles ensures that damage assessment models closely align with field observations, facilitating their validation and further improvement. Bottom of Fig. 3 provides a section of the Nashville-Cookeville tornado profile available from the NWS DAT for Wilson County, which will be investigated later in this paper. Thus, once the tornado profile and its continuous wind speed contours across a tornado's path are obtained, the next step is to determine the locations of buildings exposed to spatially map wind speeds or intensity measures (im) to individual buildings given by im_i (where i represents building index) and support detailed computational damage analysis.

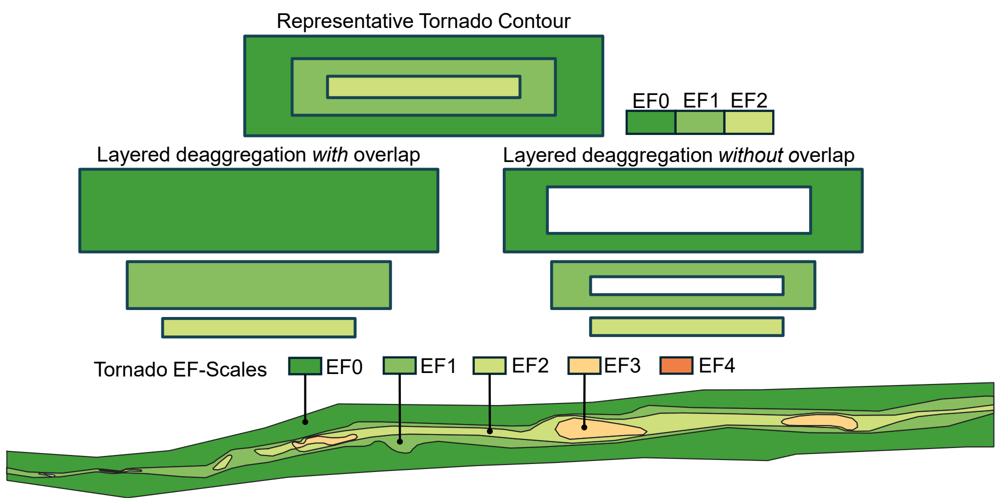

Fig. 3. (Top) Deaggregation of conceptualized gradient-based tornado profile with and without overlap of contours, and (Bottom) NWS tornado profile from Wilson County with EF contours highlighted.

3.2.2 Geolocation Mapping

There is typically a spatial mismatch between the geolocations from the open-access datasets and the field-collected data points. There are buildings for which the field survey lacks complete DS classification, while others have classifications recorded for locations situated beyond the available tornado windfield model. The objective is to leverage open-source data for community modeling as-is, without altering the original data sources or the tornado windfield model. The field and model data are matched using the geolocation from field data points to enable comparison and damage correlation analysis. While open-access data often contain duplicates and spatial discrepancies, the StEER data undergo rigorous post-processing to ensure high geospatial accuracy. Consequently, after appropriate filtering and deduplication, the NSI dataset is aligned with the StEER geolocation data using the BallTree algorithm via spatial indexing and nearest-neighbor searches. The disparities in geolocation between the exposure data and field data are mapped through this approach. This provides geospatial consistency between the datasets and facilitates accurate comparison between field and model data. As a representative example, Fig. 4 provides a schematic of the spatial mapping process linking exposure data from the NSI data and field geolocations, and the computed distances between each NSI point and its nearest field data neighbor. To minimize mapping errors, the NSI records with a spatial displacement exceeding 10 m from verified field locations were excluded. This threshold was determined through a sensitivity analysis in QGIS and Python, which revealed that distances beyond 10 m consistently introduced misalignments comparable to those illustrated in Fig. 4 with (a) and (b) highlighting the errors. The reduction in the building dataset after applying such filtering criteria is illustrated in Fig. 11.

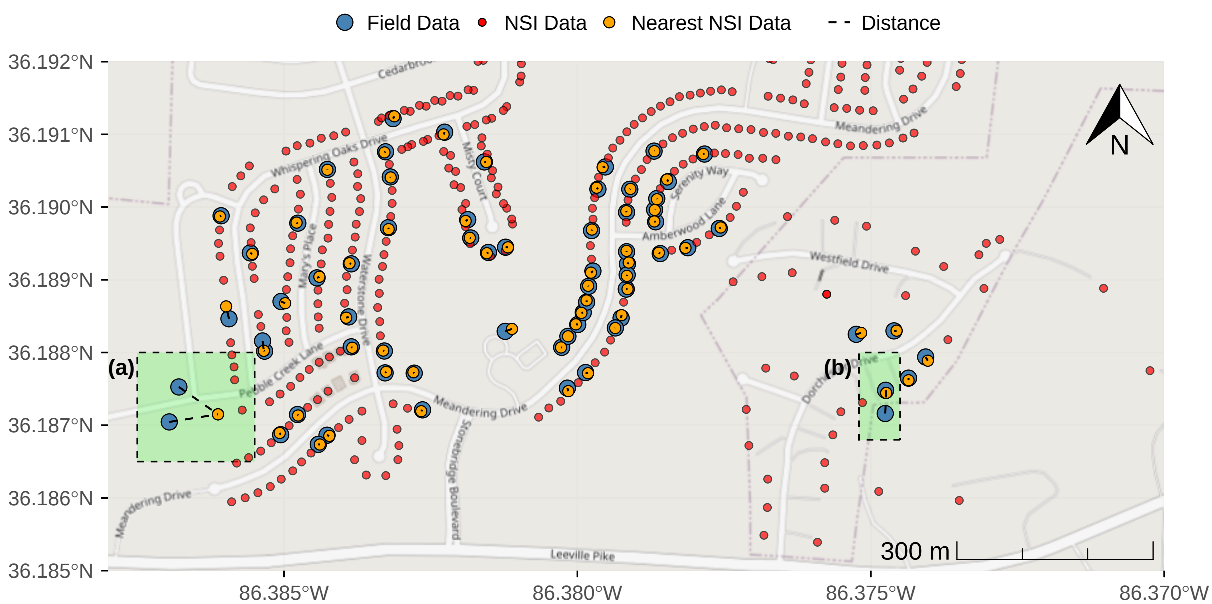

Fig. 4. Field data points mapped to the NSI dataset for an area in Wilson county to facilitate one-to-one comparison for damage analysis. (a) Illustrates location where the NSI data is absent at the ground-truth field locations; field data points are mapped to the NSI structure located at a distance exceeding 10 meters. (b) Demonstrates an erroneous mapping due to structural omission from the NSI database. A field data point is incorrectly associated with the NSI structure, which already possesses a correct mapping with another field data point.

3.2.3 Building Archetypes Mapping

Archetypes of buildings are simplified, standardized models for buildings grouped and defined under a single model when they recur and share common patterns and features, such as square footage, roof types, number of stories, occupancy type, and construction material. These features for a particular building B_i, where $i \in 1, 2, ..., n$, obtained from publicly available datasets for n buildings, are represented by a feature vector $b_i = [b_{i1}, b_{i2}, ..., b_{ic}]$ for each key attribute c. A predefined set of archetypes, A_h, is available from open-source community resilience models for l archetypes, where $h \in 1, 2, ..., l$, have their own feature set $a_h = [a_{h1}, a_{h2}, ..., a_{hd}]$ for each key attribute d. For each building, i, feature set b_i is compared to feature sets a_h of all l archetypes, and the closest matching archetype A_h is assigned to each building through a mapping function $\mathcal{M} : B_i \rightarrow A_h$ which maximizes the number of similar features.

Accurate building archetype mapping in this step is vital to preventing errors in computational community model development. However, applying building archetypes introduces limitations for tornado damage modeling in the next step. One significant challenge lies in the variability of structural performance among buildings that may share similar archetype features but differ in subtle yet critical ways, such as construction quality, maintenance condition, or retrofits—factors not captured by standard feature sets. Tornado damage models often rely on damage functions whose availability and granularity for each archetype are a controlling factor in the model's accuracy. In many cases, damage functions may be derived from sparse empirical data or expert judgment, introducing uncertainty. This is a key source of error in hindcasting tornado events, as mismatches between real-world building performance and archetype-based assumptions can lead to under- or overestimation of damage. Consequently, ensuring that representative damage functions are both available and appropriate for each archetype is critical to improving the fidelity of community-level tornado impact simulations.

3.3 Computational Community Model Development

Once the tornado hazard is characterized and building geolocations and archetypes are mapped, these elements feed into a computational model to simulate expected damage based on the relative wind speeds buildings experience at their locations along the tornado path. These provide insight into the accuracy of existing community resilience models when juxtaposed with field assessments. Finally, accurate archetype mapping enables an understanding of the specific risks and vulnerabilities of buildings and building groups, aiding decision-makers in planning for enhanced mitigation, preparedness, and recovery strategies targeted to the group of building archetypes and communities that predominantly consist of such groups.

The computational model typically relies on probabilistic analysis using fragility functions that describe the probability of a component or structure reaching or exceeding a specific LS or DS under exposure to a particular hazard intensity measure, commonly wind velocity for tornado hazards. The component-level fragilities provide the probability of a component $j \in 1, ..., m$ exceeding a certain limit state k, represented by $ls_{jk} \in 0, ..., q$, for a given hazard intensity measure im_j. The probability of exceedance can be written as

$$P\left(LS \geq ls_{jk} \mid IM = im_j\right) = f_D\left(im_j, \Theta_{jk}\right) \tag{1}$$

where, $\Theta_{jk} = \{\mu_{jk}, \sigma_{jk}\}$ is the set of parameters representing mean and standard deviation of the natural logarithm of the intensity measure, $\ln(im_j)$, respectively, and can be determined using empirical and computational approaches to fragility analysis. The fragility function f_D is described by the lognormal cumulative distribution function (CDF) of the following form

$$f_D\left(im_j, \Theta_{jk}\right) = \Phi\left(\frac{\ln(im_j) - \mu_{jk}}{\sigma_{jk}}\right) \tag{2}$$

where Φ is the standard normal CDF. To aggregate component-level limit states into a building-level limit state, we define a global mapping function $G(\cdot)$

$$LS_{ik} = G\left(\left\{LS_{jk}\right\}_{j \in \mathcal{J}_i}\right) \tag{3}$$

where $j = 1, ..., m$ refers to all possible components within a building and $\mathcal{J}_i$ refers to a specific subset of components that are part of building i. This function determines how the failure of individual components translates into building failure. Then, fragility function for building i given by $f_D(im_i, \Theta_{ik})$ can be written as

$$f_D\left(im_i, \Theta_{ik}\right) = P(LS \geq ls_{ik} \mid IM = im_i) = P\left(G\left(\{LS_{jk}\}_{j\in\mathcal{J}_i}\right) \geq ls_i \mid IM = im_i\right) \tag{4}$$

Similar to component level, building fragility f_D is described by the lognormal CDF with parameter set $\Theta_{ik} = \{\mu_{ik}, \sigma_{ik}\}$ as follows

$$f_D\left(im_i, \Theta_{ik}\right) = \Phi\left(\frac{\ln(im_i) - \mu_{ik}}{\sigma_{ik}}\right) \tag{5}$$

The mapping function $G(\cdot)$ is established to determine the overall building fragility through one of the two approaches: 1) a system failure model which assumes structural failure when any critical component fails (series or parallel failure path), and 2) a probabilistic failure model using Monte-Carlo simulation (MCS), which incorporates the interactions, dependencies, and correlations between all the components.

This facilitates calculation of the exact probability that a building is in a specific DS_k (Eq. 6), for the occurrence of any of the shaded extent of component j's damage provided in Fig. 7. Considering three limit states for building level fragility will yield four damage states, DS_0, DS_1, DS_2, and DS_3, representing *insignificant*, *moderate*, *extensive*, and *complete* damage, respectively, and calculated as follows

$$DS_k = \begin{cases} 1 - LS_0, & k = 0 \\ LS_{k-1} - LS_k, & 1 \leq k \leq q \\ LS_q, & k = q + 1 \end{cases} \tag{6}$$

In Eq. 6, the lowest damage state ($k = 0$) is the probability of not exceeding the first limit state, $1 - LS_0$; each intermediate damage state ($1 \leq k \leq q$) is the probability mass captured between two adjacent limit-state exceedance curves, $LS_{k-1} - LS_k$; and the highest damage state ($k = q + 1$) equals the probability of exceeding the last limit state, LS_q. This construction ensures that the resulting damage-state probabilities partition the full probability space and sum to unity. Then, the most probable damage state of each building, DS_{MP}, can be obtained as follows

$$DS_{MP} = \underset{0 \le k \le q+1}{\arg\max}\, P(DS_k) \tag{7}$$

$P(\cdot)$ represents an exact probability value for the building being in a particular DS_k. Unlike the LS, DS probabilities sum to one: $\sum_{k=1}^{q+1} DS_k = 1$. Then, the total number of buildings in each DS is calculated by summing the total number of buildings with DS_{MP} in each DS category.

3.3.1 DS and DoD Mapping

The EF scale estimates 3-second gust speeds at the point of damage using engineering judgment of observed field damage, combined with weather and radar data. McDonald and Mehta (McDonald and Mehta 2006) classified damage across 3 to 12 levels for 28 indicators/built environments. One such damage classification for one- and two-family residences is presented in Table 1. Studies have highlighted the advantages of using the higher-resolution structural damage assessment scale, such as DoD, over lower-resolution classifications, such as Hazards U.S. Multi-Hazard (HAZUS-MH) DSs (Nevill and Lombardo 2021), for functionality and resilience models. Field investigations can identify damage at high resolution and provide more detailed feedback to inform and update lower-resolution models. One of the cases evaluated in this study assessed building damage using DoD rather than classifying them into DSs. Based on these degrees of damage and mean wind speed within the DoD level classification, these have been mapped to the six degrees of DSs by Adhikari et al. (Adhikari et al. 2021). However, for consistency across all case studies, the DoD is mapped to the five DSs in the present study and presented in Table 2.

TABLE 1. DoD for DI_2 (one- or two-family residences)

DoD	Damage Description	Wind Speed in m/s (mph) Expected	Lower Bound	Upper Bound
0	Threshold of visible damage	29 (65)	24 (53)	36 (80)
1	Loss of roof covering material (<20%), gutters and/or awning; loss of vinyl or metal siding	35 (79)	28 (63)	43 (97)
2	Broken glass in doors and windows	43 (96)	35 (79)	51 (114)
3	Uplift of the roof deck and loss of significant roof covering material (>20%); the collapse of the chimney; garage doors collapse inward; failure of porch or carport	43 (97)	36 (81)	52 (116)
4	Entire house shifts off foundation	54 (121)	46 (103)	63 (141)
5	Large sections of roof structure removed; most walls remain standing	55 (122)	47 (104)	64 (142)
6	Exterior walls collapsed	59 (132)	50 (113)	68 (153)
7	Most walls collapsed, except small interior rooms	68 (152)	57 (127)	80 (178)
8	All walls collapsed	76 (170)	64 (142)	89 (198)
9	Destruction of engineered and/or well-constructed residence; slab swept clean	89 (200)	74 (165)	98 (220)

423 The HAZUS Hurricane Model Technical Manual (FEMA 2022), developed by the Federal Emergency Management Agency (FEMA), has standardized a methodology that provides qualitative damage descriptions associated with the five DSs, ranging from no damage (DS_0) to complete damage (DS_4). Full descriptions of damage related to the DSs for various construction classes can be found in the technical manual.

TABLE 2. DoDs mapped to DSs based on damage descriptions from field.

DoD	DS	Description
0–1	0 (None to Minor)	Minimal visible damage or no damage at all.
2–3	1 (Minor)	Minor damage to roof or siding, slight structural damage that does not compromise building's structural integrity.
4–5	2 (Moderate)	More substantial damage, such as partial roof loss and broken windows, may affect the building's usability but not functionality.
6–7	3 (Extensive)	Major structural damage, such as large roof sections being blown off, wall collapse, and load path disruptions that compromise life safety and building functionality.
8–9	4 (Complete)	Significant portions of the building collapsed or destroyed.

3.3.2 Model Evaluation Metrics

To evaluate the predictive performance of the model against field-observed data, we utilized metrics specifically suited for ordinal categorical data.

Agreement Table: To evaluate the performance of a classification model by comparing the prediction outputs against actual values, an agreement table similar to confusion matrix in computer engineering is envisioned and tailored for tornado damage assessment. This illustrates how well the model-predicted DS align with field-observed DS. Diagonal entries in the matrix indicate correct classification, while off-diagonal entries represent misclassifications. In this study, each cell (u, v) in the matrix represents percentage of field observations (F_i) in damage state k, where $k \in 0, 1, ..., q+1$, for x number of testbeds. Hence, the agreement table of dimension $(q + 1) \cdot x \times (q + 1) \cdot x$ is constructed, showcasing $q + 1$ damage state classifications for x testbeds at once, allowing for joint evaluation across both damage classification and testbeds. This facilitates comparison of damage state classification performance both within a testbed and across various testbeds, and enables identification of under- or overestimation of DSs, offering insights into the model performances and highlighting potential biases, and areas for improvement.

Quadratic Weighted Kappa (κ_w): This metric is used to evaluate the agreement between the predicted model DS and the observed field DS while accounting for the ordinal nature of the DSs. While unweighted kappa treats all misclassifications equally, κ_w accounts for the inherent ordering of the data by assigning weights to the degree of disagreement (Vanbelle 2016). It is calculated as:

$$\kappa_w = 1 - \frac{\sum_{i,j} w_{i,j} G_{i,j}}{\sum_{i,j} w_{i,j} E_{i,j}} \tag{8}$$

where $G_{i,j}$ represents the observed number of buildings in the ith field category and jth model category, $E_{i,j}$ is the expected number of buildings under chance agreement, and $w_{i,j} = \frac{(i-j)^2}{(K-1)^2}$ is the quadratic weight for a K-category system. A κ_w value of 1 indicates perfect agreement, 0 indicates agreement no better than chance, and negative values indicate agreement worse than chance. This measure provides a robust indicator of how well the model reproduces the field-observed categorical distribution of damage. This also ensures that the penalty disagreement increases according to the square of the distance between the categories. This provides a better "stress test" than a linear regression metric.

Chi-squared test: To assess the statistical significance of association between predicted and observed outcomes, the Chi-square test was utilized as a supporting diagnostic. The test should be interpreted as an association test rather than as a direct measure of agreement, calibration, or predictive accuracy. Because the field and model DS labels are paired at the building level, the Chi-square test of independence does not directly test whether the model systematically overpredicts or underpredicts damage for the same structures. Instead, it evaluates whether the cross-tabulated model and field classifications exhibit a non-random association. Assuming independence between the prediction and the field observation, the Chi-square test quantifies the extent of deviation from randomness. It indicates whether the prediction has some meaningful association with the field-observed outcomes. As a result, the Chi-square results are interpreted here alongside paired descriptive measures, including exact agreement, overprediction, underprediction, and average ordinal error, rather than as standalone evidence of predictive accuracy. A Chi-square test of independence can be performed for each testbed individually, as well as for the total, as follows:

$$\chi^2 = \sum_{r=1}^{R} \sum_{s=1}^{S} \frac{(O_{rs} - E_{rs})^2}{E_{rs}} \tag{9}$$

where r denotes the model DS, and s indicates the field DS with both $r, s \in k$, O_{rs} is the observed frequency in model r and field s, E_{rs} is the expected frequency under independence, R is the total DS count from model, and S is the total DS count from the field.

The null hypothesis (H_0) assumes the predicted DS classifications are independent of the observed field DS classifications, meaning any association is by chance or randomness. Then, it follows that the alternative hypothesis (H_1) indicates a statistically significant association between model and field DS classification, indicating that the model captures underlying, non-random patterns in the observed data. A low p-value (here $p < 0.05$) will lead to rejection of (H_0) in favor of (H_1), which supports the presence of statistical association but does not, by itself, establish predictive accuracy or transferability. If the p-value is high, there is insufficient evidence to reject (H_0), which suggests that the model's predictions may be independent of, or weakly associated with, field conditions.

IMPLEMENTATION OF PROPOSED APPROACH IN US COMMUNITIES

This section presents the implementation of the proposed approach for US communities, focusing on its integration within the IN-CORE framework. It begins by outlining how field DS is systematically mapped to IN-CORE's existing DS definitions to ensure interoperability and consistency. Following this, the implementation of fragility models is described, highlighting how these models are incorporated into the IN-CORE environment to support hazard analysis and resilience assessment.

IN-CORE (IN-CORE 2024a) is an open-source platform for community testbeds modeling that integrates community data, physics-based models of systems with socio-economic interdependencies to provide quantitative resilience metrics for community-level decision-making (Roohi et al. 2020). IN-CORE enables community data integration into the platform to produce an accurate community model, support the projection of various resilience strategies, and optimize disaster resilience planning and post-disaster recovery. These testbed models must be transferable across communities to facilitate easy integration with decision- and policymaking frameworks. By utilizing structured building inventories and hazard datasets aligned with platform-specific semantics (IN-CORE 2024b), the framework enables users to assign archetypes and execute damage analyses. For tornado hazards, IN-CORE currently estimates damage by assuming a uniform wind speed distribution within discrete EF-scale contours. While this approach effectively captures expected damage values at the community scale, it doesn't fully reflect field observations, and localized under- or overestimation may occur depending on the building's geospatial position relative to EF intensity boundaries.

4.1 The NSI exposure dataset mapping to IN-CORE archetypes

To support exposure modeling, building archetypes are mapped using publicly available data sources to ensure consistency with the standardized archetype definitions in the open-source community resilience model. (Memari et al. 2018) proposed and employed a multitude of them for the Joplin testbed, as detailed in Table 3. Such an approximate representation of diverse structural types in the community ensures that the unique vulnerabilities of each structure type are accounted for in the damage assessment. The exposure layer is modeled on the county-level building inventory dataset obtained from the NSI, with mapping via Table 4, despite the buildings observed in the field being mostly single-family residential (SFR), to achieve consistent, comparable outcomes across communities. 19 distinct archetypes were developed by various authors, and Memari et al.

TABLE 3. 19 archetypes from Joplin testbed and their descriptions.

Archetype	Building Description
1	Residential wood building, small rectangular plan gable roof, 1 story
2	Residential wood building, small square plan, gable roof, 2 stories
3	Residential wood building, medium rectangular plan, gable roof, 1 story
4	Residential wood building, medium rectangular plan, hip roof, 2 stories
5	Residential wood building, large rectangular plan, gable roof, 2 stories
6	Business and retail building (strip mall)
7	Light industrial building
8	Heavy industrial building
9	Elementary/middle school (unreinforced masonry)
10	High school (reinforced masonry)
11	Fire/police station
12	Hospital
13	Community center/church
14	Government building
15	Large big-box
16	Small big-box
17	Mobile home
18	Shopping center
19	Office building

Individual buildings are mapped to the 19 archetypes from the Joplin testbed (Memari et al. 2018) as presented in Table 4. The mapping is based on various characteristics such as the number of stories, square footage, and building features. The table presents the codes and descriptions of various building types from the NSI dataset and maps them as closely as possible to the 19 archetypes numbered 1-19. RES-1SNB and the following 5 building types are separated into residential archetypes according to the number of stories and floor area. In contrast, RES1-3*, which are 3-story archetypes, are mapped to archetype 5 from Joplin due to a lack of archetype availability for accurate mapping. No multi-family residential structures with more than 2 units were identified within the tornado damage path considered in this study; RES3A which is the multifamily building with 2 units is the only building type within the tornado map and hence is mapped to the largest available residential archetype (Archetype 5). The 19 standard IN-CORE archetypes do not include dedicated representations of multi-family residential buildings. Consequently, the exclusion of multi-family buildings with more than 2 units reflects the availability of building inventory within the affected area. Other buildings are categorized and mapped by their specific use, such as banks, hospitals, schools, and strip malls. It facilitates applying the available fragilities to other similar communities comprising various building types by assigning appropriate archetypes based on structural characteristics.

Future applications of the proposed framework to inventories containing multi-family residential buildings as well as other under-represented archetypes in the available fragility sets would require the development of dedicated fragility models and archetype mappings. Multi-family structures are distinct structural systems than single-family residential buildings, and their response to tornado-induced loads cannot be reliably represented using existing single-family archetypes. Developing and calibrating tornado fragilities for these building classes remains an important area for future research.

TABLE 4. Mapping of building types from the NSI to the 19 Joplin archetypes.

Building Type Code	Description	Archetype Code(s)
RES1-1SNB	Single Family Residential, 1 story, no basement	1, 3
RES1-1SWB	Single Family Residential, 1 story, with basement	1, 3
RES1-2SNB	Single Family Residential, 2 story, no basement	2, 4, 5
RES1-2SWB	Single Family Residential, 2 story, with basement	2, 4, 5
RES1-3SNB	Single Family Residential, 3 story, no basement	5
RES1-3SWB	Single Family Residential, 3 story, with basement	5
RES2	Manufactured Home	17
RES3A	Multi-Family housing 2 units	5
COM1	Average Retail	18
COM2	Average Wholesale	7
COM3	Average Personal & Repair Services	18
COM4	Average Professional Technical Services	19
COM5	Bank	19
COM7	Average Medical Office	19
COM8	Average Entertainment/Recreation	16
IND1	Average Heavy Industrial	8
IND2	Average Light Industrial	7
IND5	Average High Technology	8
AGR1	Average Agricultural	1
REL1	Church	13
GOV1	Average Government Services	19
EDU1	Average School	9

The mapping provides essential information for comprehensive risk assessment, resilience analysis, and damage experienced by each building. Buildings exposed to the tornado along the defined paths in the tornado profile will have their DSs determined by the fragility functions based on the wind speeds they experience. This setup streamlines damage analysis by enabling efficient dataset retrieval, ensuring accurate analysis. Fig. 5 illustrates the mapping between the NSI occupancy types and the IN-CORE archetypes.

Fig. 6 presents an overview of all case study areas and depicts the distribution of the cleaned and post-processed archetypes within each case study area across the three tornado paths (see Section 5).

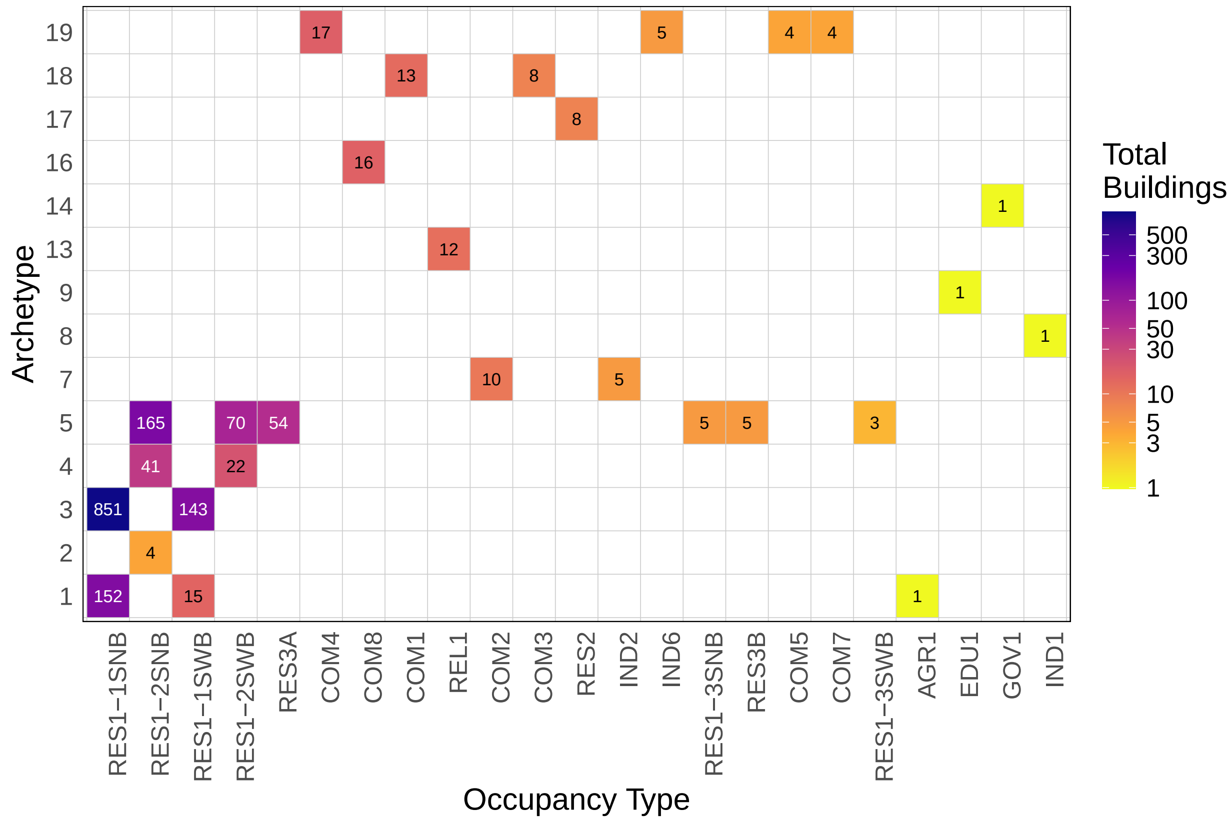

Fig. 5. Heat map of the building *archetypes* matched to the NSI *occupancy types* according to Table 4.

4.2 Field DS mapping to IN-CORE DS definitions

The definitions of the DS in the IN-CORE model include DS_0, DS_1, DS_2, and DS_3, representing *insignificant*, *moderate*, *extensive*, and *complete* damage, respectively. In contrast, field observations define DS_0 to DS_4 as *no damage*, *minor damage*, *moderate damage*, *severe damage*, and *destroyed*. For consistency in the analysis of DS definitions from the model, the field DSs are adjusted so that the combined field DS_0 and DS_1 match DS_0 from the model; and other DSs from the field, DS_2, DS_3, and DS_4, are shifted down to DS_1, DS_2, and DS_3, respectively. These are summarized in Fig. 7. We will adhere to the four DS classifications from IN-CORE in subsequent analysis and discussion sections. This adjustment enables a more accurate comparison between the field data and the model output.

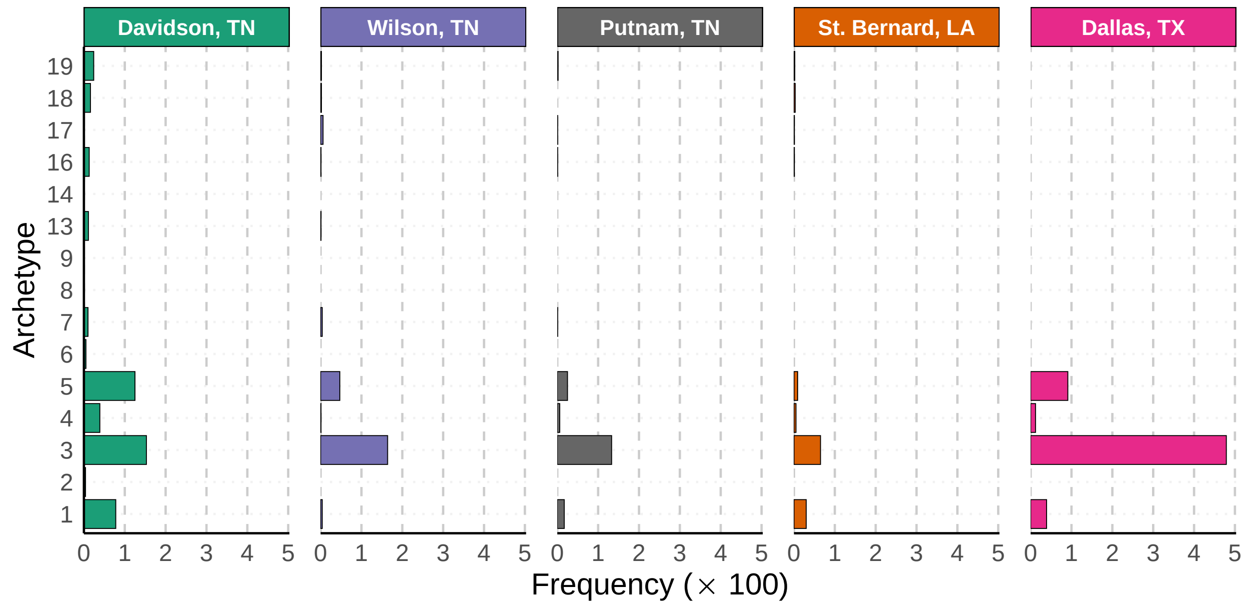

Fig. 6. Distribution of the 19 building archetypes mapped across all the investigated areas.

This remapping is a pragmatic necessity for reconciling the five-state field scale with the four-state model scale, but it carries implications that should be acknowledged as a source of epistemic uncertainty. Collapsing the field "no damage" (DS_0) and "minor damage" (DS_1) categories into a single model DS_0 removes the ability to distinguish truly undamaged buildings from lightly damaged ones, and can therefore mask subtle model performance issues at the lowest damage levels. For example, a model that have similar probabilities for buildings being in no-damage and minor-damage categories would appear to perform correctly under the merged category. Because the quadratic weighting of κ_w penalizes disagreements by the square of the ordinal distance, single-level boundary effects introduced by the remapping have a bounded influence on the reported statistics. The merged lowest category should be interpreted with this limitation in mind, and quantifying the sensitivity of the results to alternative remapping schemes is identified as future work.

4.3 Fragility Assignment

The state-of-the-art fragility function datasets from the IN-CORE platform are utilized to investigate tornado damage. The fragilities are engineering-derived functions assembled from

Model Damage Sates	Field Damage States		Illustrative Examples	Presence or Extent of Failure				
				Roof or Wall Cover	Window or Door	Roof or Wall Substrate	Roof Structure	Wall Structure
0 Minor	0 None or Very Minor	No Visible Exterior Damage		0%	No	No	No	No
	1 Minor	Damage Confined to Envelope		>2% and ≤15%	1	No	No	No
1 Moderate	2 Moderate	Load Path Preserved, but Significant Repairs Required		> 15% and < 50%	> 1 and ≤ the larger of 3 and 20%	1 to 3 panels	No	No
2 Extensive	3 Severe	Major Impacts to Structural Load Path		> 50%	> the larger of 3 and 20% and ≤ 50%	>3 and ≤ 25%	≤ 15%	No
3 Complete	4 Destroyed	Total Loss, Structural Load Path Compromised beyond Repair	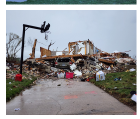	> 50%	> 50%	> 25%	> 15%	Yes

Notes: Shaded cells are buildings considered to be in the higher damage state.

Fig. 7. *DS* classifications from model and field assessment [adapted from (Vickery et al. 2006b)] and their mapping based on their respective model and field *DS* definitions.

mechanics-based analyses, component-to-system simulations, design provisions, and ASCE 7 standard-based structural assumptions (Wang and van de Lindt 2021b; Wang and van de Lindt 2022; Memari et al. 2018). The fragility functions are mapped to individual buildings within the community by developing mapping rules that identify specific archetypes. Mapping according to Table 4 is used to examine whether the IN-CORE damage assessment framework, whose credibility has been extensively supported through the 2011 Joplin testbed, remains applicable to other communities. Limit-state fragility parameters for 19 archetypes are synthesized from various works (Wang and van de Lindt 2021b; Wang and van de Lindt 2022; Memari et al. 2018) and implemented in IN-CORE for tornado damage analysis.

A damage assessment model is developed in IN-CORE to simulate and analyze the impact of tornadoes on three different communities. Tornado profiles obtained from NWS DAT are processed by discretizing the EF contours into a structure compatible with the platform. The geolocation of building inventories from the NSI data is mapped to the field data geolocation using spatial indexing and nearest-neighbor search techniques for accurate comparison. The *DS* definitions of the field observations from the STEER team are adjusted to align closely with the model definitions. DSs are juxtaposed, and correlations between the field-observed and model-predicted states are analyzed using Quadratic Weighted Kappa, κ_w and agreement table. Three case studies are conducted to highlight the model's performance across different communities, identify discrepancies between the model and field data, and suggest areas for improvement.

4.4 Design level mapping

To account for structural variability, buildings were mapped to fragility functions based on the design levels (DLs) defined in Table 5 (Wang and van de Lindt 2022). DLs represent the hierarchy reinforcements for key structural elements applied to residential archetypes, ranging from basic to advanced configurations. The associated fragility identifiers and parameters were sourced directly from the IN-CORE platform. The fragility parameters are summarized in Table 12 of Appendix I, while the associated fragility identifiers for the DL are as follows:

- DL_1: 5e4ca44f9e2c59000178984d
- DL_2: 5e4ca5299e2c590001789854
- DL_3: 5e4ca5f89578290001e5905b

TABLE 5. Retrofit strategies of residential buildings in different DLs.

Structural elements	Description	DL_1	DL_2	DL_3
Roof covering	Asphalt shingles	X	X	–
	Clay tiles	–	–	X
Roof sheathing nailing pattern	8d C6/12	X	–	–
	8d C6/6	–	X	X
Roof-to-wall connection type	Two 16d toenails	X	–	–
	Two H2.5 clips	–	X	X

CASE STUDIES AND RECONNAISSANCE SURVEY

This study evaluates building resilience and damage states by analyzing three significant tornado events across the South-Central United States: the 2020 Nashville-Cookeville tornado, the 2022 Arabi tornado, and the 2015 Dallas tornado. These cases were selected to represent two higher-intensity tornado classes (EF3 and EF4) and to capture the structural variation and construction practices, as well as leveraging the authors' direct involvement in post-event field investigations and prior modeling efforts in these regions, ensuring the use of validated, high-fidelity data. The absence of an EF5 event in the additional testbeds (beyond the original Joplin EF5 tornado case study) is attributed to (1) the rarity of EF5 tornado occurrences and (2) the lack of direct author involvement in a recent EF5 event. This limitation is not expected to materially affect the analysis, as EF5 tornadoes are exceedingly rare, and even in such events, only a small number of structures typically experience EF5-level damage. The majority of the damage path is generally subjected to EF4 or lower wind intensities.

This selection enables an initial cross-community comparison and provides valuable insights into framework performance across these diverse event conditions and community characteristics, while establishing a foundation for future validation using a broader range of tornado environments. The interpretations of generalization and transferability should be understood within these constraints before additional datasets are integrated.

The Nashville-Cookeville event provides a large-scale data set across multiple counties (Davidson, Wilson, and Putnam). In contrast, the Arabi event offers a unique perspective on modern construction performance, as many structures in the area were rebuilt in accordance with the 2006 IRC codes following Hurricane Katrina (Roueche et al. 2023). Finally, the 2015 Dallas event serves as a high-intensity benchmark, with peak winds reaching 180 mph. Together, these events allow for a robust comparative analysis of structural fragility. Table 6 provides a comprehensive summary of the spatial characteristics, peak wind speeds, and the resulting human and economic impacts for each event (NCEI 2024; NOAA 2020; Maas et al. 2024).

Fig. 8 illustrates the trajectories and intensity profiles of the three selected tornado events. This illustrates the directionality, geographic extent, and varying damage swaths for each case study, providing the foundation for the subsequent vulnerability analyses.

To accurately categorize the structural variability of the building stock across the three study regions, DLs were assigned based on the local building code adoption. The study utilized the

TABLE 6. Summary of Tornado Events and Impacts

Event	Date	EF (mph)	Tornado Path (L, W, Direction)	Economic Loss	Human Impact
Nashville-Cookeville	2020	4 (165)	(96.56 km, 1.45 km, Eastward)	~$1.6 Billion	25 Deaths, 300+ Injuries
Arabi	2022	3 (160)	(18.51 km, 0.30 km, Northeastward)	~$30 Million	1 Death, 2+ Injuries
Dallas	2015	4 (180)	(20.99 km, 0.50 km, Northeastward)	~$3 Billion	10 Deaths, 468 Injuries

specific adoption history of the International Building Code (IBC) and the International Residential Code (IRC) within the target jurisdictions. For example, improvements in construction practices in Arabi are reflected in the assignment of DL_2 fragilities to buildings constructed using the IRC 2006 code and later (construction era 2007-present). Key structural parameters investigated for demarcating included roof-to-wall connections (RWC) and roof deck attachment (RDA). Table 7 synthesizes the code adoption history and the recommended DL mapping.

TABLE 7. DL Assignments Based on Regional Building Code Adoption and Key Structural Parameters

Jurisdiction(s)	Construction Era	Code Reference	Structural Features	DL
Coastal	2007 – Present	IRC 2006 & later	RWC: 1; RDA: 8d; Shutters: 1	2
St. Bernard Parish	Pre-2007	Unknown / Legacy	RWC: 0; RDA: 6d; Shutters: 0	1
Interior	Post-2018	2018 IRC	RWC:1; RDA: 8d Ring-Shank Nails	2
Wilson, Davidson,	2014/15 – 2018	IRC 2012	RWC: 1; RDA: 8d	1
Putnam, Dallas	Pre-2014	IRC 2006 & earlier	RWC: 0; RDA: 8d/6d	1

5.1 Reconnaissance Process: Preliminary National Weather Service (NWS) Survey

The left figure in Fig. 9 illustrates the discrepancy between field data and NWS tornado windfield, and depicts the damage identified from a detailed survey of the Arabi tornado, which extends beyond the tornado contour established by a preliminary NWS survey. The detailed field survey provided more extensive damage information, including damage to some buildings outside the NWS tornado profile. The right figure shows misalignment between DS classification and the

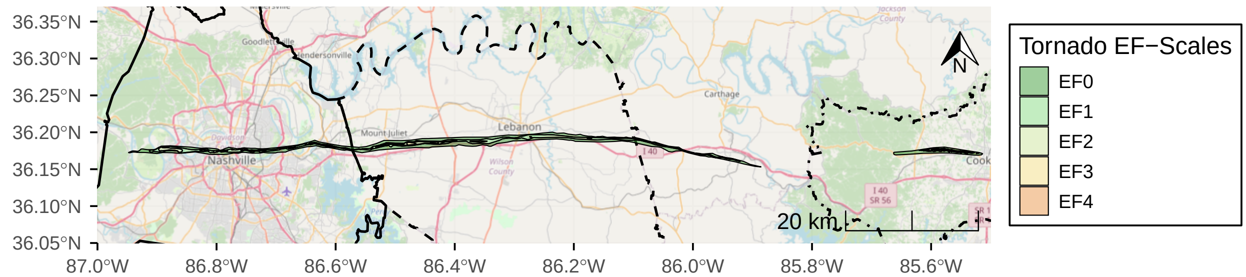

(a) Nashville-Cookeville tornado path with county boundaries: Davidson (——), Wilson (- - -), and Putnam (-·-·).

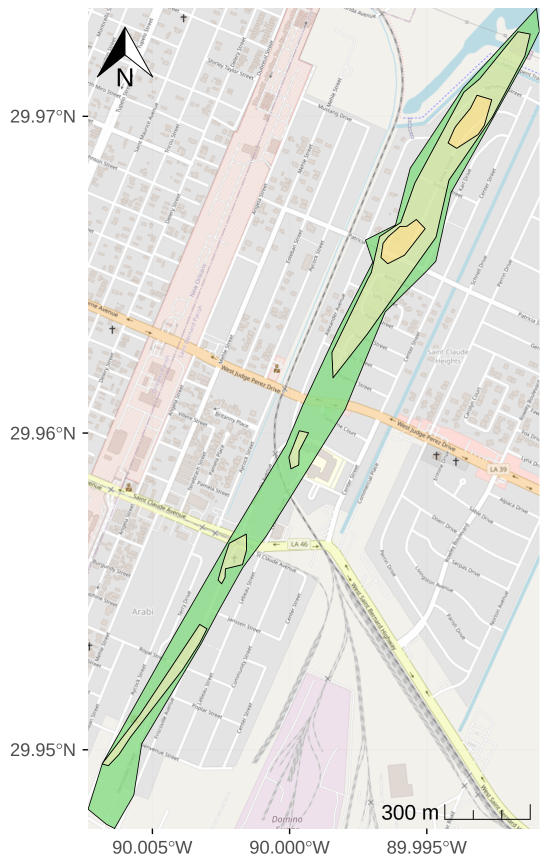

(b) Arabi tornado path

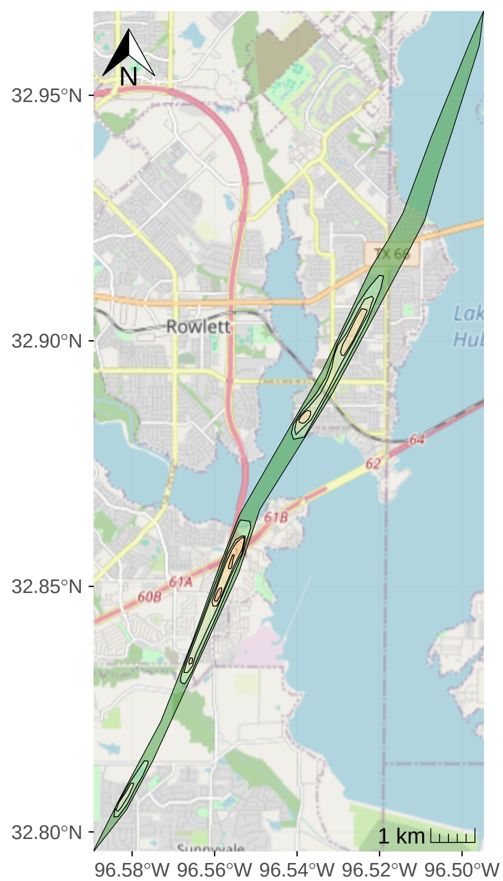

(c) Dallas tornado path

Fig. 8. Tornado path with EF-profiles and associated case study locations. The figure highlights differences in path length and intensity measure to contextualize variations in tornado impact. Case study locations are labeled to correspond with detailed descriptions in the main text.

EF-wind speed expectation. Buildings are classified as higher DS even though they lie within lower EF-scale contours. An uncalibrated hazard layer significantly affects the model's damage output. This underscores the importance of a detailed field investigation. The high-resolution data obtained from door-to-door field assessments and UASs, as well as public input and recordings in the aftermath of the event, provide greater accuracy for damage assessment. The contours could be refined with comprehensive information.

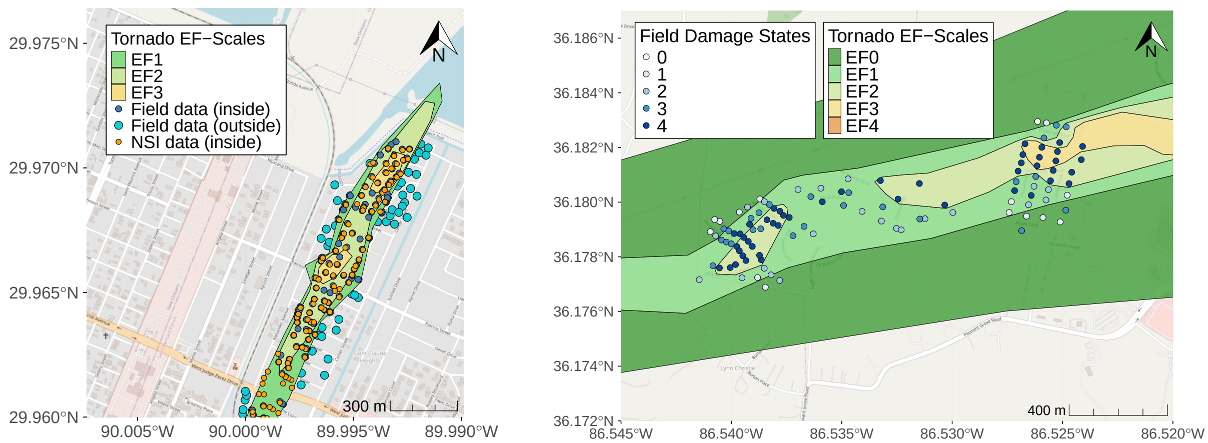

Fig. 9. Disparity in StEER field data and NWS tornado contours: (left) NSI and StEER collected field data points for St. Bernard NWS tornado windfield, and (right) buildings with field DS classification within the tornado windfield in an area of Wilson county.

5.1.1 *Comprehensive Post-Event Reconnaissance by StEER*

The field reconnaissance team carefully selected clusters of buildings along the tornado's path to assess and capture the tornado's intensity gradient in both the transverse and longitudinal directions. For all the tornado events considered in the study, the StEER Field Assessment Structural Team (FAST) yielded various findings, including DS and DoD information. For example, for the Tennessee-based tornadoes, the field investigation included door-to-door assessments leveraged with UAS for clusters of buildings in Nashville, Mount Juliet, Lebanon, and Cookeville, along with street view imagery along the entire track of the tornado (Wood et al. 2024). The reconnaissance sampled pre-selected building clusters along the tornado path to capture variations in both the transverse and longitudinal directions. A recent study examining surveyor agreement and discrepancies found that agreement between evaluators was low for less severe damage but worsened with increasing damage severity (Merhi et al. 2026). While the damage state categorization was obtained from a single surveyor, the individual criteria for damage rating (e.g., % roof cover damage, % window/door damage, etc) was later separately quantified by a team of data librarians using all available imagery (aerial, street-level panoramic, and StEER photos), and the original damage rating was verified against the component level damage percentages to ensure consistency. However, an important consideration is that the final post-processed dataset comprised a single damage categorization. A formal inter-coder reliability assessment was not feasible in the present study due to the lack of overlapping observations.

Right panel of Fig. 9 highlights inconsistencies in EF-contours derived from the field damage investigation by NWS and the field data from the StEER survey. The StEER survey classifies several buildings as DS_4 that lie outside the damage contours, representing the most intense EF-scale, which in this case is EF-3, as identified by NWS from its preliminary survey. This implies that the tornado model used for analysis may underestimate or overestimate damage, depending on the accuracy of the EF contours used to drive it. These findings provide an opportunity to continuously update the database as new information becomes available, thereby enhancing resilience models and informing accurate, effective decision-making.

In recent construction practices, reconnaissance identified several concerns regarding the disparity in the strength of building components along vertical load paths (straps and anchors are used at some connections, and toenails at others). Poor structural performance was observed in reinforced, unreinforced, and precast concrete construction, while mobile/manufactured homes, whose tornado vulnerability is assumed to be sufficiently high, were less affected. A lack of tornado shelters was observed even for critical infrastructures such as schools and government facilities, which suffered significant structural and non-structural damage. This observation also raised significant concerns about code-compliant housing units, including ineffective transfer of load from the structure to the foundation, with only the structure's gravity load resisting the uplift force. This variability is not captured within the fragility-based models. This section examines the disparity between field and model data and whether the model captures these uncertainties.

The model's damage assessment categorizes building damage into 4 DS categories, while field damage for 4 counties is categorized into 5 DSs and for 1 county into 10 DoDs. Both DS and

DoD classification information are available for the three communities investigated, while only one classification is available for the other two. The number of field investigated buildings are 274, 200, 558, 210, and 718 for Wilson, Putnam, and Davidson Counties, St. Bernard Parish, and Dallas County, respectively. A summary of the total DoD and DS classification for the buildings is visualized in Fig. 10.

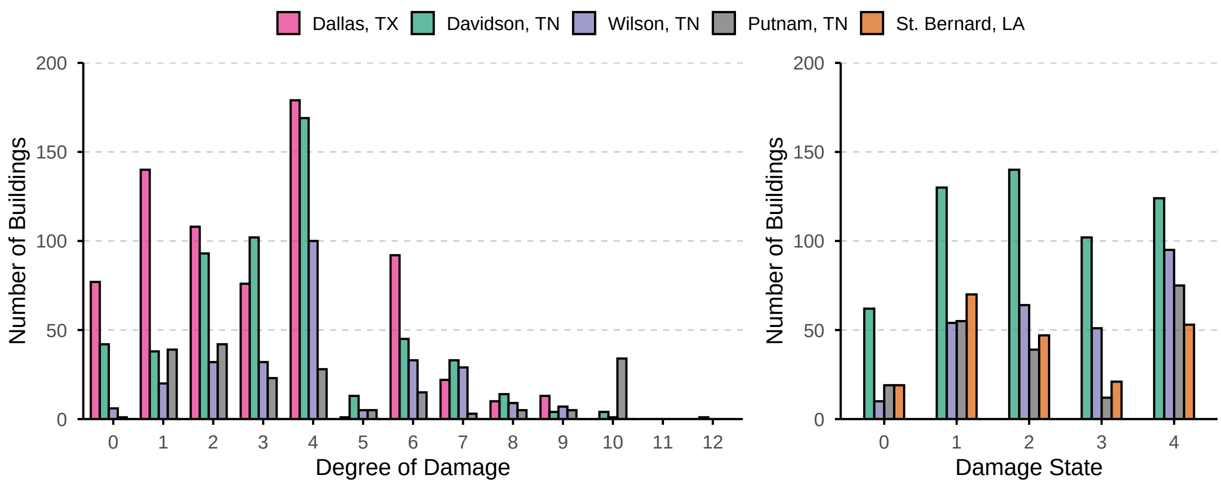

Fig. 10. Number of buildings classified into (left) DoD, and (right) DS categories from field observation for the case study areas. St. Bernard field investigation did not provide DS classification, while Dallas field investigation provided only DoD classification. For the other three counties, both the DS and DoD values are available.

After filtering for data points within the tornado path only, and geolocation mapping with the NSI dataset, the number of samples considered for model analysis reduced to 232, 186, 481, 116, and 621 observations, respectively. The reduction in sample space is illustrated in 11. The data is then processed to conduct archetype mapping and DoD to DS mapping.

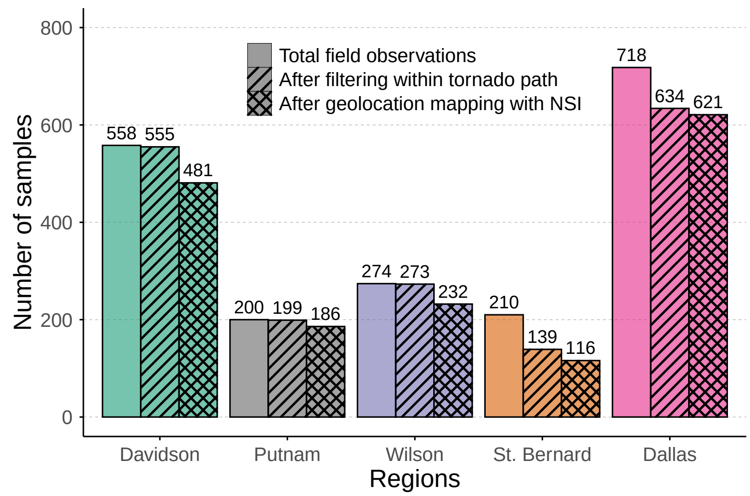

Fig. 11. Sample size pre- and post-processing.

Fig. 12 presents the distribution of archetypes across damage states, together with the average EF-scale rating experienced by each archetype within the corresponding damage state. The results indicate that buildings frequently reach higher damage states without necessarily being subjected to peak EF-scale wind speeds, underscoring the variability in structural performance across the community's building stock.

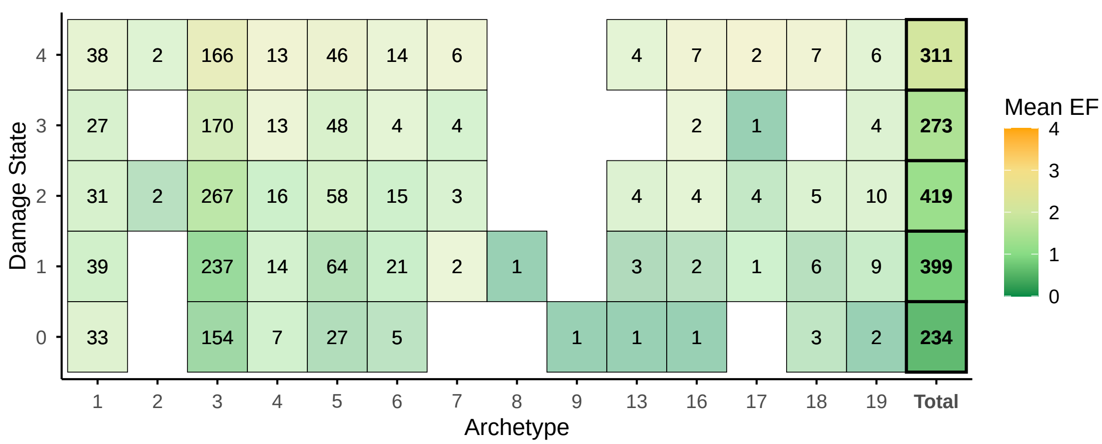

Fig. 12. Heat map showing damage state experienced by the buildings representing each archetype. The cells include the total count of the buildings, and colors show the average EF-scale experienced by each archetype in that damage state.

5.2 Spatial Scale Effects in the 2011 Joplin Tornado Case Study

The May 22, 2011, Joplin tornado represents one of the most devastating tornado disasters in U.S. history. Hence, the Joplin tornado has been the most extensively studied testbed for tornado hazard assessment. For tornado damage analysis and resilience planning through hindcasting, the Joplin testbed has been extensively used in the literature. While previous studies (Attary et al. 2018; Wang and van de Lindt 2021a) have reported good correlation between IN-CORE models calibrated for Joplin and aggregate observed damage, our more granular, multi-event validation reveals that these Joplin-calibrated models do not consistently maintain predictive accuracy or transferability when applied to other contexts or at the individual building scale.

6,893 unique buildings are obtained after extracting the buildings from the NSI dataset that lie inside the given Joplin tornado contour (Fig. 13). The results in Table 8 are obtained from damage analysis for these exposure inventory using DL_1 fragilities.

TABLE 8. Number of buildings in each damage state (DS) for DL_1 fragilities.

DS	Building Counts, N (%)
DS_0	38 (0.56%)
DS_1	531 (7.7%)
DS_2	521 (7.56%)
DS_3	5,803 (84.19%)

The number of buildings that are completely damaged and destroyed (5,803) using DL_1 fragilities is substantially overestimated compared to field observations (43% of total buildings were destroyed (Aghababaei et al. 2020a)), while remaining comparable to estimates reported by other similar models (88.9% of total buildings were completely damaged (Wang and van de Lindt 2021a)). This comparison indicates that community-scale model outputs can appear similar across modeling studies while still differing substantially from field-observed damage. For the same general Joplin testbed context, the fraction of buildings predicted to be completely damaged ranges from roughly 43% in field-based estimates to 84% under DL_1 fragilities here and 88.9% in the model of Wang and van de Lindt (Wang and van de Lindt 2021a). The spread between field observation and model estimates is consistent with the fragility set and design-level assumption being major contributors to aggregate damage estimates within the IN-CORE framework, while not isolating them from uncertainties in hazard and exposure representation. However, investigation into two independent sets of field-observed datasets, Dataset 1 with 488 buildings, Joplin-A, (Fig. 14a) and Dataset 2 with 74 buildings, Joplin-B (Fig. 14b), illustrates that a more granular, and sparse building selection for DS classification will have field investigation biases and variability that model will not be able to capture. Following geolocation mapping of the field data to the NSI dataset, 352 buildings were successfully matched and retained for subsequent analysis. Damage classifications for these buildings in the Joplin tornado path are obtained from (Roueche et al. 2024c).

TABLE 9. Transposed marginal sensitivity analysis for Joplin-A showing DS classifications by row and assumed structural DL by column, compared with the observed field-data marginal distribution (Lombardo et al. 2015). Each of the columns summarize the Joplin-A records used for the design-level sensitivity analysis ($N = 352$) compared with actual Field Data. This table is a marginal sensitivity summary rather than a paired agreement matrix.

Damage State	Assumed DL			Field Data
	1	2	3	
DS_0	0	17	54	99
DS_1	2	13	3	54
DS_2	2	108	148	144
DS_3	348	214	147	55

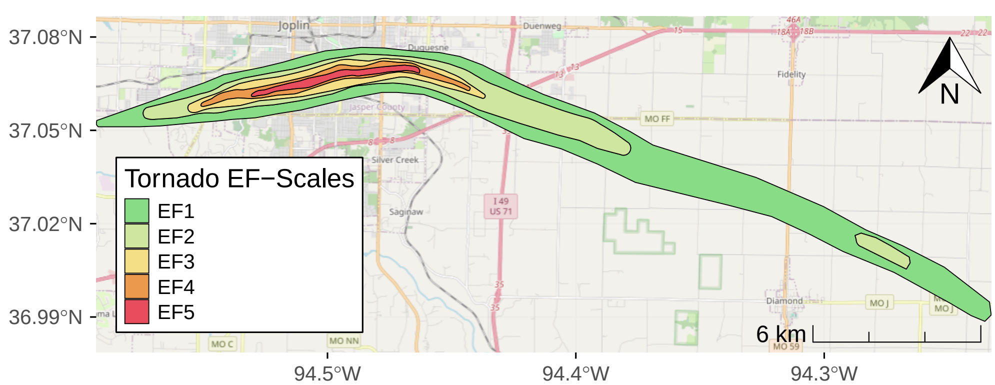

Fig. 13. Joplin tornado profiles with EF-Scale contours

Implementing all three design-level fragilities for the wind speed estimations by Lombardo et al. (Lombardo et al. 2015) to obtain exact DS classification according to Eq. 7, the sensitivity results are gathered for Joplin-A (Table 9). This demonstrates that with a constant hazard field, the assumed fragilities play a significant role in predicting the damage states of the buildings. Under the assumption that buildings are at DL_1, the model yields only higher-order DS classifications. Given DL_2 and DL_3 fragilities, a broader distribution of DS is observed, reflecting more dispersed DS and closer alignment with field investigation. These results demonstrate that the integration of archetype mapping and hazard fields yields statistically significant predictive outcomes at the community scale. However, damage state (DS) predictions fail to capture empirical field observations at high resolution scale, regardless of the design-level fragility assumptions applied to the building stock. DL_1 and DL_2 overestimated the damage to the buildings, while DL_3 underestimated the higher DS. The results demonstrate the limitations of fragility models, uncertainties in building capacity assumptions, and shortcomings of simplified DS classification based on maximum likelihood estimation.

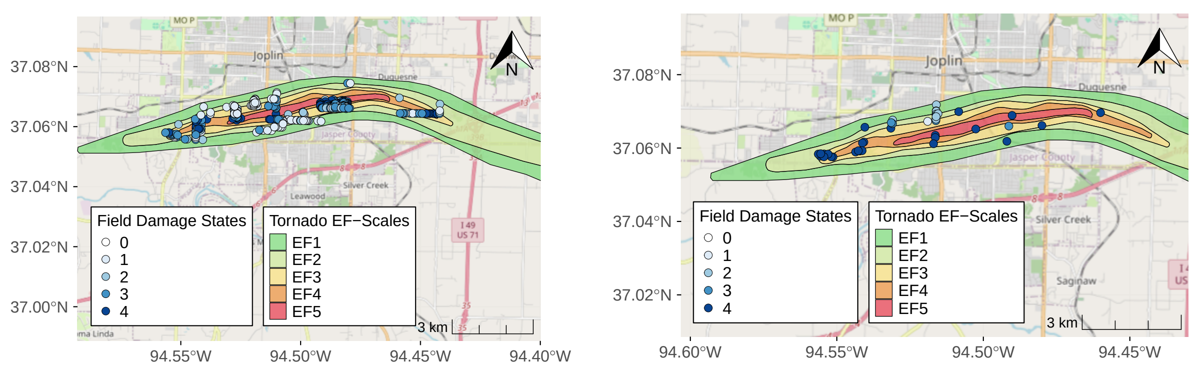

(a) Joplin-A **(b)** Joplin-B

Fig. 14. Dataset for Joplin at two levels of resolutions from the field observation.

Fig. 15 presents a field and model comparison matrix where the colored boxes represent the count of geolocationally matched model and field buildings that fall within the respective DS classification. It illustrates a large uncertainty in damage prediction when the two cases are considered. The model, which performs relatively well at scale, does not seem suitable for a more granular analysis. The model's large-scale hindcasting and prediction performance does not translate well to a more granular, randomized, and sparse analysis. The results indicate that the model predominantly predicts DS_3 across both datasets. As the sample size increases, the model exhibits greater dispersion (Table 8), highlighting the inherent discrepancies in its output due to variations in field assessment resolution.

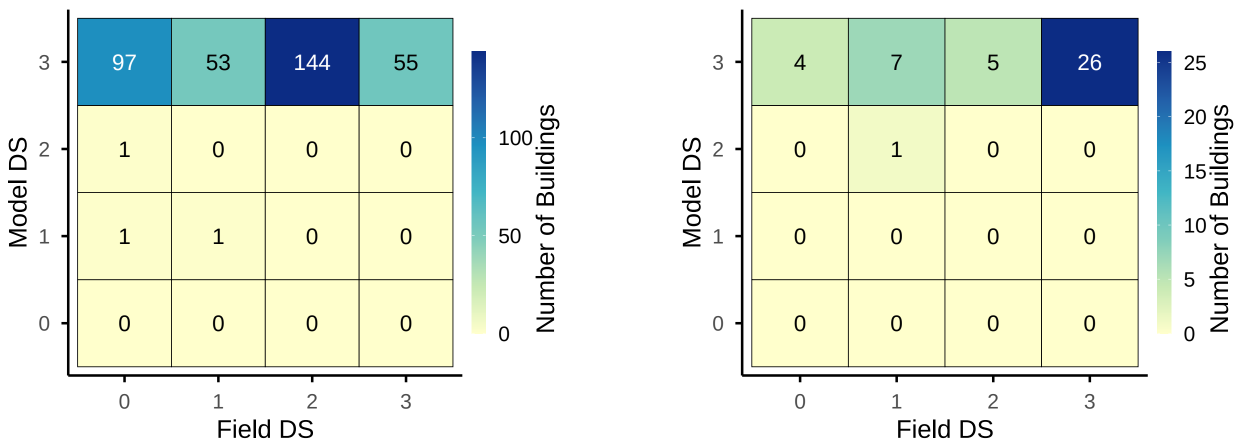

Fig. 15. Comparison of field-observed and model-predicted DS for two spatial resolutions in Joplin. For both resolutions, the model predictions exhibit systematic overprediction.

Similarly, the presented case studies have varying levels of granularity - the number of investigated buildings ranges from 43 to 621. These generate highly uncertain predictions, as explained in the subsequent section. This internal consistency among models that nonetheless diverge from field data reinforces the need for the rigorous, field-anchored transferability and validation analysis pursued in this study.

RESULTS AND DISCUSSION

Table 10 provides all DS counts from field data and model output, specifically for building inventories geolocally mapped to field inventories. This approach allows a pairwise comparison between field-observed and model-predicted data and provides more intuitive insight into the model's improvement. Fig. 16 provides a graphical color-map comparison of the DSs from the field data and the model output. As the figure shows, the model DSs do not accurately represent the ground truth. Some buildings were cataloged in the field as DS_1, whereas the model identifies them as DS_0. The model tends to overestimate the number of buildings with no damage compared to field data across all areas, even with the earlier mapping.

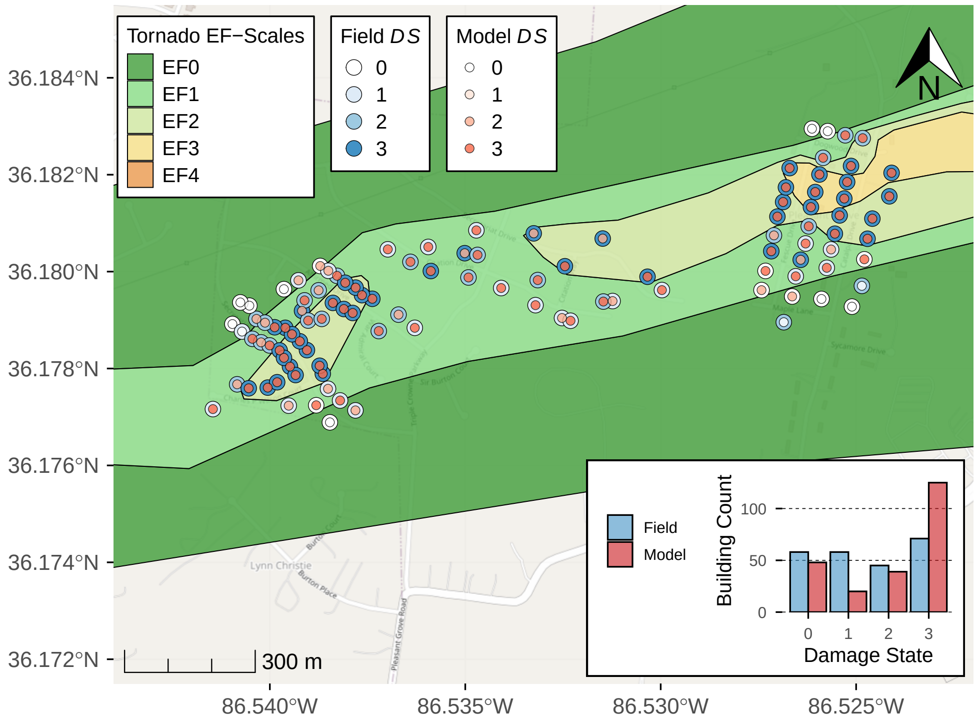

Fig. 16. Model outcomes compared to field observed DS within their EF contours. The histogram illustrates the distribution of residential buildings across DSs in Wilson County, comparing empirical field observations with model predictions.

Further investigation of DS probabilities and spatial configuration of buildings reveals critical insights into the performance and limitations of current fragility-based predictive frameworks. Although global discrepancies are evident, localized discrepancies in which the difference in DS assignments between field-observed and model-predicted states exceeds 2 ordinal DS levels, $|DS_{field} - DS_{model}| \geq 2$, suggest systematic errors attributable to fragility functions. In Fig. 17(b), a building mapped to archetype 5 is highlighted, for which the crossover in LS fragilities between LS_0 and LS_3 demonstrates the inconsistency, resulting in the probability of being in DS_2 being negative. This is further compounded by a near identical probability values for two of the maximum DSs within a probability margin of less than 10%, $|\Delta P(DS)_{max_{1,2}}| < 0.1$, where 1 and 2 denote the first and second maximum probability of being in any of the four DS for a building. This forces a DS_3 prediction via Equation 7's maximum probability criterion, resulting in a deviation of three levels from ground truth. The absence of appropriate dispersion constraints across limit states prevents consistent separation among fragilities, thereby allowing overcrossing and probabilistic ambiguity between neighboring damage states ($P(DS_0) \approx P(DS_3)$). The maximum-likelihood decision, therefore, assigns an erroneously higher damage level, despite the secondary probability better matching field evidence. Fig. 17(c) demonstrates another case of classification error due to near identical probabilities ($P(DS_0) \approx P(DS_1)$), $|DS_0 - DS_1| = 0.04$, resulting in DS_{model} prediction 1 state higher than DS_{field}. And Fig. 17(d) illustrates a dominant case where the model predicts DS_0 with P(DS_0) = 0.65 with higher certainty yet systematically underestimates DS by two states ($DS_{field} = 2$). This highlights how even predictions with high probability of being in DS are erroneous due to deficiencies in the fragility models.

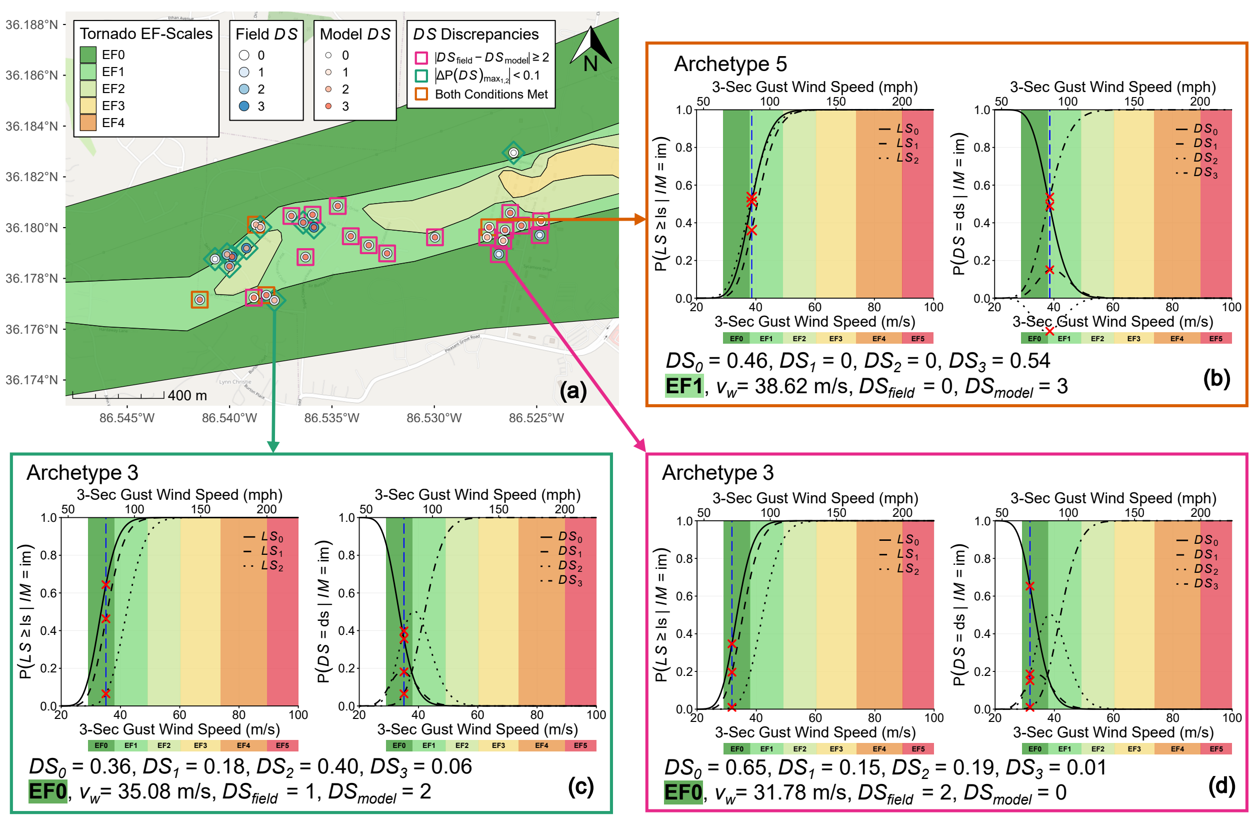

Fig. 17. Comparative analysis of model-predicted vs field-observed damage states. (a) Spatial distribution of significant discrepancies ($|DS_{field} - DS_{model}| \geq 2$) and small probability difference between two maximum probable DS. (b) Archetype 5 with model error ($DS_{model} = 3$ vs $DS_{field} = 0$) caused by improper dispersion parameters of the adjacent limit states and resulting in crossover. (c) Misclassification due to a narrow margin (<10%) between the two most probable damage states. (d) High confidence model misprediction where model predicts $DS_{model} = 0$, $P(DS_0) = 0.65$, yet underestimates DS_{field} by two states.

TABLE 10. Number of buildings in particular DS for the case study areas

Damage State	Davidson Field	Davidson Model	Wilson Field	Wilson Model	Putnam Field	Putnam Model	Arabi Field	Arabi Model	Dallas Field	Dallas Model
DS_0	157	97	58	46	68	45	28	9	322	90
DS_1	125	47	58	16	35	7	31	13	170	1
DS_2	97	66	45	49	10	29	14	32	107	78
DS_3	102	271	71	121	73	105	43	62	22	452

Table 11 illustrates the model's predictive performance using quadratically weighted Kappa (κ_w) and shows that it varies significantly across the studied communities. The highest agreement was observed for Putnam and Wilson, where the model effectively captured the distribution of observed damage states. Using the Landis and Koch scale (Landis and Koch 1977), the model's performance was categorized into perfect (0.81-1.00), substantial (0.61-0.80), moderate (0.41-0.60), fair (0.21-0.40), and slight/poor (0.00-0.20). The model exhibited moderate agreement in Putnam and Wilson ($\kappa_w \approx 0.59$ and 0.43, respectively), fair agreement in Davidson and St. Bernard ($\kappa_w \approx 0.37$ and 0.22, respectively), and slight to poor agreement in Dallas and Joplin ($\kappa_w \approx 0.12$ and 0.01, respectively), where systematic overprediction was most prevalent. The statistical outcome highlights uncertainties inherent in the event with the influence of local factors, including variations in construction practices, building age and code adoption, housing stock characteristics, maintenance conditions, terrain and topographic effects, vegetation and surrounding exposure conditions, as well as differences in tornado intensity distributions and damage assessment practices. The low p-values and the quadratic weighted kappa indicate a statistically significant, non-random association between model predictions and field-observed damage, but they do not, by themselves, constitute evidence of operational readiness; transferability to heterogeneous tornado environments requires further multi-event validation before operational deployment.

A percent agreement table in Fig. 18 demonstrates a direct one-to-one comparison between field-observed and model-predicted DS across different communities. This facilitates descriptive evaluation of building-level model performance relative to field data, including exact matches and directional misclassifications. Each cell in the matrix quantifies the percentage of buildings in the given category for both the model prediction and field observation. Higher values (percentages)

TABLE 11. Weighted Kappa and Error Analysis by Community

Community	N	κ_w	Agreement Strength	p-value	Exact %	Under %	Over %	Average Error
Wilson	232	0.43	Moderate	< 0.001	42.67	14.66	42.67	0.50
Putnam	186	0.59	Moderate	< 0.001	59.14	6.99	33.87	0.57
Davidson	481	0.37	Fair	< 0.001	38.46	10.60	50.94	0.76
StBernard	116	0.22	Fair	< 0.001	36.21	17.24	46.55	0.65
Dallas	621	0.12	Slight	< 0.001	15.30	2.58	82.13	1.71
Joplin-A	352	0.01	Poor	0.10	15.91	0.00	84.09	1.55
Joplin-B	43	0.03	Poor	0.24	60.47	0.00	39.53	0.74

Note: Agreement strength for κ_w value - perfect (0.81-1.00); substantial (0.61-0.80); moderate (0.41-0.60); fair (0.21-0.40); and slight/poor(0.00-0.20). Average Error denotes the mean signed ordinal error, calculated as $DS_{model} - DS_{field}$; positive values indicate net overprediction. Reported κ_w values are point estimates and should be interpreted cautiously, especially for smaller samples such as Joplin-B.

along the diagonal indicate strong agreement between field observations and model predictions, while off-diagonal elements indicate misclassifications. The figure also reveals a substantial number of buildings above the diagonal, indicating overestimation, where the model predicts higher damage states than observed. From the figure, it can be observed that when the field classification is DS_0 or DS_1, the model classification varies across buildings from DS_0 to DS_3. In contrast, for DS_2 and DS_3 field classifications, the model-predicted DS is mostly concentrated at DS_3.

The model also shows greater certainty in classifying low (DS_0) and high (DS_3) damage levels than intermediate damage levels. As evident in the results, all model-predicted DS_2 values are nearly negligible across communities, indicating the model's uncertainty in classifying mid-range building damage. The matrix also shows that the model prediction, compared to the field DS, is within ±2 DS. A ±1 has also been reported as the variability in the field DS classification. Accordingly, exact-agreement percentages should be interpreted as a strict and conservative measure of building-level agreement because single-level field-label variability can shift observations across adjacent DS boundaries. The present analysis summarizes exact matches and directional errors, but it does not propagate this field-label uncertainty through a formal tolerance-based metric. This shows potential biases and inconsistencies across different communities.

The model's tendency to concentrate predictions at the extreme states, and in particular its

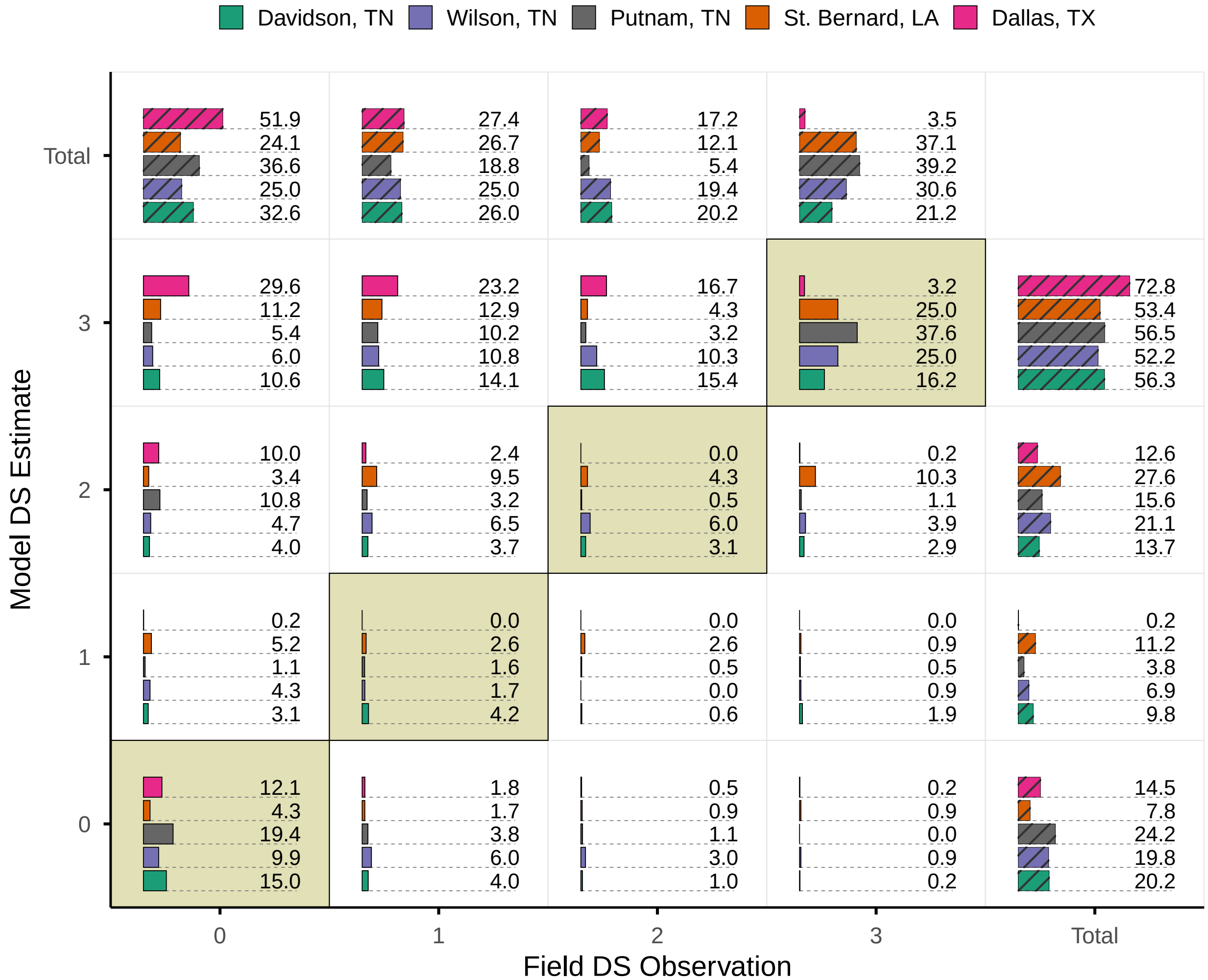

Fig. 18. A percent agreement table showing field-observed and model-estimated classification across four DS classes for the case study areas. Each cell represents the percentage of buildings that are in both the field and model DS classifications for a particular community. Higher values on the diagonal suggest stronger model performance, while off-diagonal values demonstrate misclassification patterns.

predominant assignment of DS_3 at the wind speeds characteristic of these EF3–EF4 events, can be traced to the way the underlying fragilities are constructed rather than to the exposure or hazard inputs. Three mechanisms contribute. First, the damage states are derived as differences between adjacent limit-state curves (Eq. 6); when the three limit-state curves are closely spaced and steep over the relevant wind-speed range, the intermediate-state probability bands (DS_1, DS_2) become narrow and rarely dominate, so the most-probable-state criterion (Eq. 7) collapses onto DS_0 below the cluster and DS_3 above it. Second, several archetypes exhibit limited or no dispersion separation between limit states, and in some cases crossover, which produces near-degenerate probabilities between non-adjacent states and forces the argmax toward DS_3 even when intermediate damage is more physically plausible (illustrated in Fig. 17). Third, the DL_1 design level assigns weak vertical-load-path connections, so that once wind speeds exceed the steep portion of the fragilities, exceedance of the highest limit state becomes overwhelmingly likely. Together these factors indicate that the DS_3 bias is primarily an artifact of fragility-curve shape and limit-state spacing, compounded by the design-level assumption, rather than of how wind speeds are mapped to buildings. This points to constraining limit-state dispersion and enforcing monotonic separation between curves as concrete avenues for model improvement.

A key source of epistemic uncertainty in the damage analysis stems from potential misassignment of both the archetypes as well as DL to the testbed building inventories. Hence, a sensitivity analysis was conducted on archetype assignments. The sensitivity analysis presented herein provides an initial quantification of the uncertainty introduced by archetype assignment decisions. Due to a limited number of available archetypes from IN-CORE, classification inconsistencies were encountered during multi-family archetype mapping, where post-hoc filtering was required to resolve ambiguous assignments. Fig. 19 demonstrates the percentage of buildings in any given DS assigned for three cases - (a) when all buildings within the tornado path are assigned a single archetype, (b) when actual mapping is considered, and (c) actual field DS data. The largest percentage point (pp) difference shows the most divergent DS for each state. Putnam model predictions behaves relatively well compared to others with Dallas showing the largest deviations from field data. This suggests that the uncertainties associated with archetype mapping have only a minor influence on overall DS classification, and the existing fragility functions do not fully capture variability in vulnerability across archetypes, reducing the influence of archetype-specific assignments on the predictions.

The “minor influence” of archetype assignment should be interpreted carefully and is not in tension with the larger discrepancies observed in overall model performance. Fig. 19 does show visible variation between the single-archetype and actual-mapping cases (most noticeably for DS_0

and DS_3), but this variation is small relative to the gap between either model configuration and the field data. In other words, switching archetypes moves the predicted distribution far less than the amount by which the predictions already deviate from observations. The reason is that the available archetype fragilities are clustered in vulnerability over the EF3–EF4 wind-speed range considered here, so that reassigning a building from one archetype to another rarely changes its most-probable damage state. These results are consistent with the fragility functions themselves and the design-level assumption being major contributors to the observed error, while archetype misassignment appears to be a secondary, though non-negligible, contributor.

Dallas warrants specific attention because it exhibits the largest deviations from field data ($\kappa_w \approx 0.12$, 82% overprediction) and because design-level misassignment could not be ruled out. Several characteristics of this testbed plausibly compound the general fragility limitations. The 2015 Garland–Dallas event struck a heterogeneous, largely pre-2000 metropolitan building stock whose construction practices, roof-to-wall connection details, and code vintage may not be well represented by the residential archetypes and design-level assumptions used in deriving the available fragilities. The field inventory for Dallas is also dominated by lower observed damage states (Table 10: 322 field DS_0 and 170 field DS_1 of 621 buildings), so the model's systematic concentration at DS_3 produces especially large overprediction precisely where most buildings sustained little damage. Finally, the design-level sensitivity analysis indicates that assigning a higher DL fits the observed Dallas distribution more closely, but this should be interpreted as a design-level identifiability limitation rather than proof that a higher DL is known to represent the building stock. These factors, heterogeneous construction, a low-damage-dominated inventory, and possible DL underassignment, together explain why Dallas is a particularly challenging case.

A sensitivity analysis was conducted by considering the building stock in all the communities to be in either of the DLs. Figs. 24 - 26 in the Appendix illustrate these points. The transition from overestimation to underestimation of DSs between DL_1 and DL_2 highlights a fragility-based sensitivity threshold within the model. This shift indicates that the effective wind resistance of the building inventory's structural elements cannot be accurately represented by a single, discrete DL.

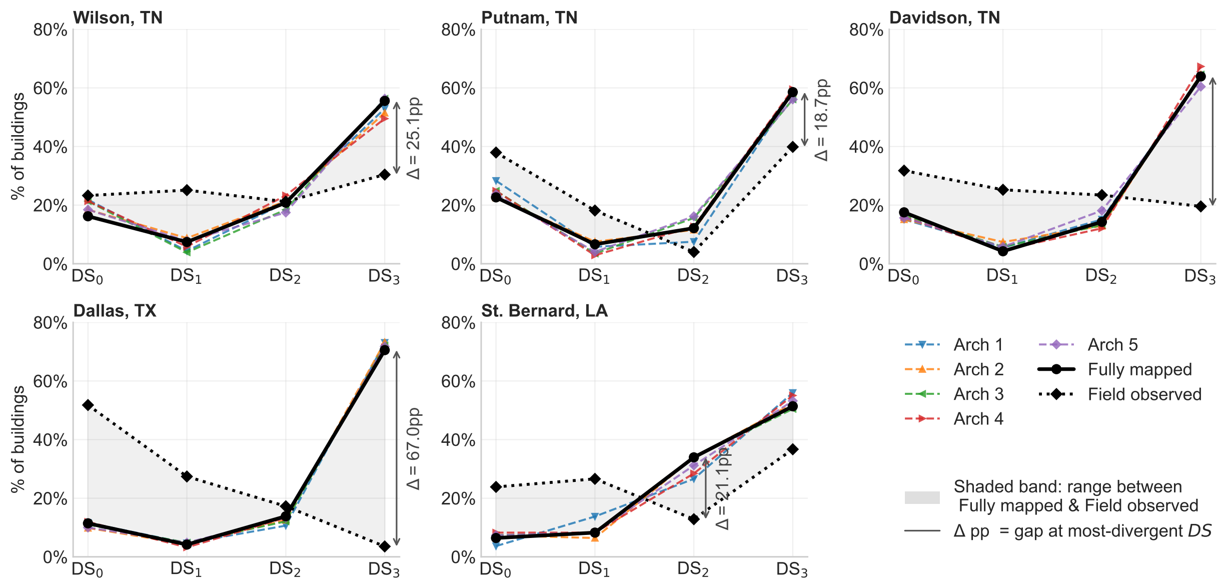

Fig. 19. Sensitivity analysis of archetype fragility assignments for residential archetypes, the dominant building inventory class, across five representative counties.

Rather, the building stock exhibits an intermediate structural capacity that exceeds the baseline DL_1, but lacks the enhanced structural modification of DL_2. Hence, applying both the rule-based DL classification (see Table 7) and the homogeneous DL results in either overestimation or underestimation of the systems' physical vulnerability.

Fig. 20 indicates rejection of H_0 in five communities, providing evidence of statistical dependence between the model and field classifications. This result suggests that the model classifications are not random with respect to field observations. However, the Chi-square statistic is an association measure and does not account for the paired building-level structure of the data, the ordinal distance between damage states, or the direction of prediction error. Davidson County, for example, has a large χ^2 value indicating strong statistical association, but only fair agreement from the weighted-kappa result ($\kappa_w = 0.37$). Thus, the Chi-square result is treated as a supporting indication of non-random association, whereas predictive performance is evaluated primarily using κ_w, exact agreement, underprediction, overprediction, and average ordinal error.

Overall, the model-predicted damage states do not fully reproduce the field observations; the magnitude and probable sources of these discrepancies are examined in the following section.

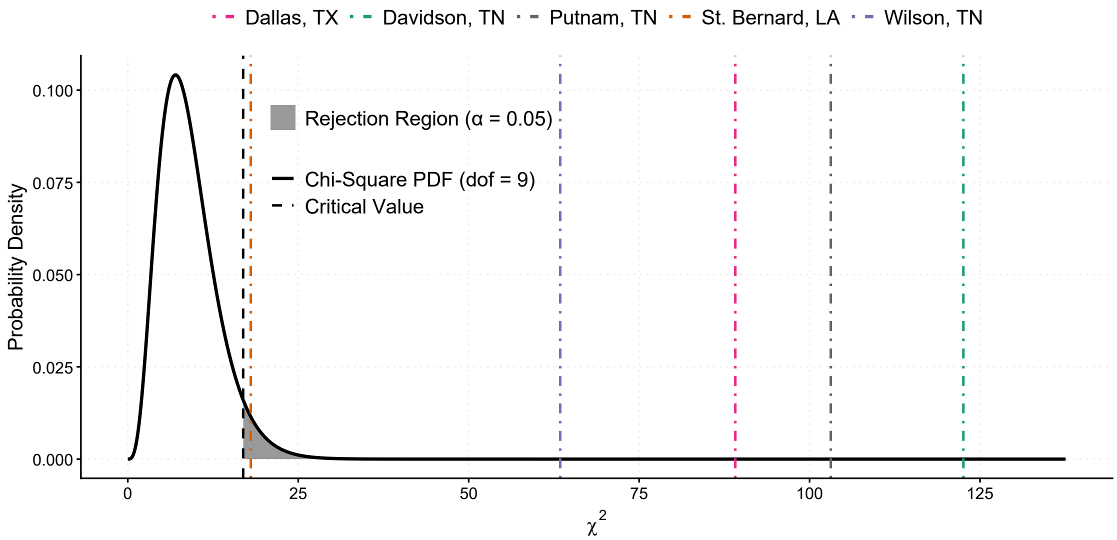

Fig. 20. Chi-square hypothesis test based on the predicted and actual DS classification. H_0 was rejected for all five primary case-study communities (Joplin, whose smaller datasets are not significant, is excluded here), suggesting significant dependence but not, by itself, predictive accuracy.

DISCUSSION ON MODEL PERFORMANCE, TRANSFERABILITY, AND REAL-WORLD IMPLICATIONS

The comparison of field observations with model predictions across multiple tornado-affected communities reveals both the capabilities and limitations of archetype-based fragility models in community-level damage assessment. The model consistently over-predicts higher damage states, indicating that the current predictions are not fully transferable without significant revision. Several potential contributors require further exploration to identify their relative importance: 1) the epistemic and aleatory uncertainties in the analytical framework for obtaining the fragility functions for various archetypes (e.g., assumptions about tornado loads), 2) imprecise information from the open-access dataset on both exposure (building inventory) and hazard (tornado), 3) uncertainty in field damage assessment, 4) geographic coverage of field investigation (samples may not be perfectly representative of the true distribution of damage states), and 5) secondary damage sources such as debris impact and missile penetration not considered in the model. Prediction mismatches at spatial resolution are also observed, showing the model's uncertainty at a granular level.

More broadly, design-level identifiability, most evident in the Dallas testbed, compounds these limitations. The Dallas results show that a design level can fit the observed field distribution more closely without proving that the same design level is the correct physical representation of the building stock; consequently, design-level misassignment cannot be ruled out as a contributing factor.

For practice, these findings imply that archetype-based tornado fragility models are best used as community-scale screening tools accompanied by explicit uncertainty bounds, rather than as building-level predictors, until they are validated and updated against local field data. Establishing reliable building-level prediction is a prerequisite for using such models to guide mitigation, preparedness, and code-related decisions for individual communities.

CONCLUSION

This paper presented an iterative, multi-stage framework for quantifying modeling error and evaluating the transferability limitations of archetype-based fragility models when applied beyond their original risk contexts, coupling post-event reconnaissance, open-access exposure and hazard modeling, computational damage analysis, and one-to-one comparison of predicted and observed damage states. Existing fragility functions, archetypes, and design levels are applied as-is, without community-specific calibration, so that each newly surveyed community contributes additional, as-is evidence on model performance. Five tornado-affected new community testbeds spanning three EF3–EF4 events (Davidson, Wilson, and Putnam Counties from the Nashville–Cookeville event; St. Bernard Parish from the Arabi event; and Dallas County from the Dallas event) were developed to assess predictive accuracy across distinct regional, community, and tornado-intensity conditions. Rather than assuming broad transferability, the framework applied existing archetype-based fragility models. Model performance was evaluated at both the community and individual-building scales by integrating open-access exposure (NSI) and hazard (NWS DAT) data with StEER post-event reconnaissance, and by quantifying discrepancies between predicted and observed damage states using agreement tables, the quadratic weighted kappa, exact agreement, directional overprediction and underprediction, and average ordinal error.

Three principal conclusions emerge. First, the existing fragility models, in their current form, are not transferable across heterogeneous tornado environments without significant, field-informed revision. Building-scale agreement proved highly inconsistent; the quadratic weighted kappa ranged from moderate ($\kappa_w \approx 0.59$ for Putnam) to negligible ($\kappa_w \approx 0.01$ for Joplin), and was accompanied by systematic overprediction concentrated in the highest damage state. Second, aggregate community-scale agreement, on which prior Joplin validations have predominantly relied, masked substantial individual-building errors; non-random association between predicted and observed damage does not, by itself, establish predictive accuracy or operational transferability. Third, a meaningful share of the discrepancy appears consistent with limitations in the construction and application of the fragility functions, including insufficient dispersion separation, limit-state crossover, instability of the most-probable-state assignment, and the discrete design-level assumption, while remaining subject to additional uncertainties in hazard and exposure representation. Collectively, these findings extend prior validation work by demonstrating that high-resolution, building-level validation is a prerequisite for, rather than a corollary of, community-scale correlation, and they delineate the specific limitations that must be resolved before archetype-based models can be deployed operationally across diverse communities.

The stronger implication is that applying archetype-based models beyond their original development and validation context should be treated as requiring either the development of community-specific fragility functions or, at minimum, a rigorous field-informed updating process anchored to local evidence before the predictions are used for decision-making. Concretely, achieving full transferability requires a structured multi-event updating architecture that revises fragility functions across diverse building inventories and geographic regions through Bayesian updating or other statistically grounded approaches as new StEER and NSI reconnaissance datasets become available.

Future work should target the deficiencies identified here along three fronts. Methodologically, limit-state dispersion should be constrained and monotonic separation enforced between adjacent fragility curves to eliminate crossover and resolve the higher-DS classification bias, ideally supported by physics-based wind-field modeling and quantification of the DoD-to-DS remapping trade-offs. From a data perspective, higher-resolution field investigations and finer design-level, archetype, and damage-state definitions are needed to enable accurate exposure modeling and reliable fragility assignment, combined with Bayesian, field-informed updating of fragility parameters using locally collected reconnaissance data. Finally, broadening the evaluation to additional events, inventories, and intensity ranges, including EF5 events and under-represented building classes such as multi-family residential, together with the integration of socio-economic, demographic, and infrastructure interdependencies, is essential to deliver a generalized, decision-ready framework for community resilience and mitigation policy.

ACKNOWLEDGEMENTS

The authors acknowledge financial support from the University of Nebraska–Lincoln, the Durham School of Architectural Engineering and Construction, and the Future of Building Industry (FoBI) seed grant. This research was also supported in part by the National Science Foundation under Grant No. 2431053. The authors would also like to express our gratitude to the anonymous reviewers for their thorough evaluation and constructive suggestions, which significantly improved the quality of this manuscript.

DECLARATION OF GENERATIVE AL USE

During the preparation of this work, the authors used large language models (LLMs) to assist with grammatical corrections and to improve language clarity and readability. These tools were not used as a substitute for the authors' critical thinking, expertise, or evaluation. All AI-assisted outputs were carefully reviewed and verified for accuracy, completeness, and impartiality, and the authors take full responsibility for the final content.

DATA AVAILABILITY

The codes that support the findings of this study are available from the corresponding author upon reasonable request.

APPENDIX I. FRAGILITIES PARAMETERS FOR DESIGN LEVELS 1 AND 2

Table 12 presents a comprehensive summary of the fragility parameters (μ and σ) for 19 building archetypes considered under Design Levels 1 and 2, providing a comparative view of damage susceptibility across design categories.

TABLE 12. Comprehensive summary of fragility parameters (μ and σ) for 19 building archetypes across Design Levels 1 and 2.

Archetype	Design Level 1						Design Level 2					
	LS_0		LS_1		LS_2		LS_0		LS_1		LS_2	
	μ	σ	μ	σ	μ	σ	μ	σ	μ	σ	μ	σ
1	3.560	0.14	3.630	0.13	3.680	0.14	3.850	0.12	3.980	0.11	4.160	0.13
2	3.530	0.13	3.590	0.13	3.680	0.13	3.760	0.12	3.910	0.11	4.170	0.12
3	3.510	0.13	3.570	0.13	3.740	0.12	3.770	0.12	3.920	0.11	4.230	0.12
4	3.650	0.13	3.710	0.13	3.760	0.13	3.870	0.12	4.000	0.11	4.280	0.12
5	3.650	0.13	3.700	0.13	3.640	0.15	3.880	0.12	3.980	0.11	4.060	0.14
6	3.625	0.11	3.895	0.11	4.075	0.21	3.625	0.11	3.895	0.11	4.075	0.21
7	3.695	0.10	3.785	0.10	3.865	0.10	3.695	0.10	3.785	0.10	3.865	0.10
8	3.565	0.14	3.965	0.15	4.135	0.19	3.565	0.14	3.965	0.15	4.135	0.19
9	3.745	0.11	3.895	0.10	4.175	0.12	3.745	0.11	3.895	0.10	4.175	0.12
10	3.735	0.11	3.895	0.11	4.265	0.12	3.735	0.11	3.895	0.11	4.265	0.12
11	3.895	0.12	4.045	0.12	4.185	0.19	3.895	0.12	4.045	0.12	4.185	0.19
12	3.785	0.09	4.165	0.09	4.355	0.09	3.785	0.09	4.165	0.09	4.355	0.09
13	3.655	0.11	3.875	0.11	4.145	0.17	3.655	0.11	3.875	0.11	4.145	0.17
14	3.555	0.11	3.815	0.11	4.035	0.13	3.555	0.11	3.815	0.11	4.035	0.13
15	3.560	0.12	4.020	0.12	4.250	0.12	3.560	0.12	4.020	0.12	4.250	0.12
16	3.460	0.12	4.090	0.12	4.240	0.12	3.460	0.12	4.090	0.12	4.240	0.12
17	3.665	0.12	3.795	0.11	3.895	0.12	3.665	0.12	3.795	0.11	3.895	0.12
18	3.635	0.12	3.875	0.10	4.055	0.17	3.635	0.12	3.875	0.10	4.055	0.17
19	3.675	0.12	3.905	0.11	4.165	0.17	3.675	0.12	3.905	0.11	4.165	0.17

APPENDIX II. LIMIT STATES AND DAMAGE STATES

Fig. 21 shows the LS fragilities for the first five archetypes (residential wood-frame buildings). Fig. 21 presents the DS curves that are constructed from the provided LS curves in Fig. 21. Fig. 22 demonstrates (for Archetype 1) visually how the LSs are translated into the probability of a building being in a given DS for a given wind speed.

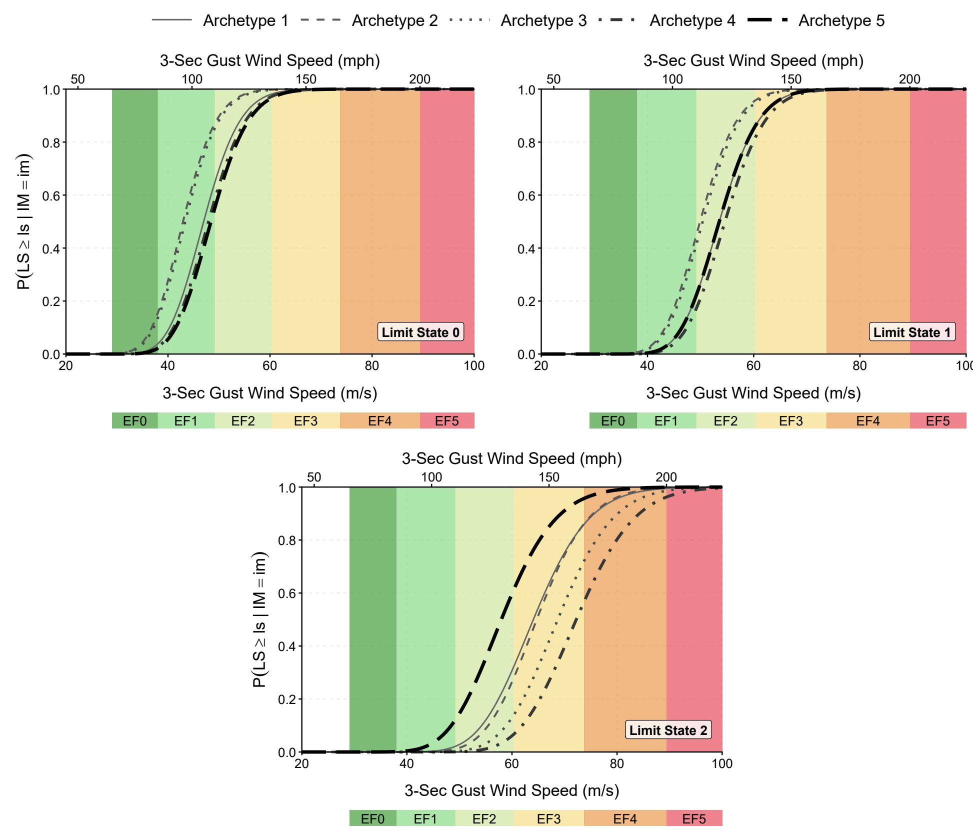

Fig. 21. Fragility curves (DL_2) for five residential archetypes from IN-CORE, showcasing probability of exceedance for three limit states. The color profiles representing EF-scales are consistent with the tornado contour plots within the paper.

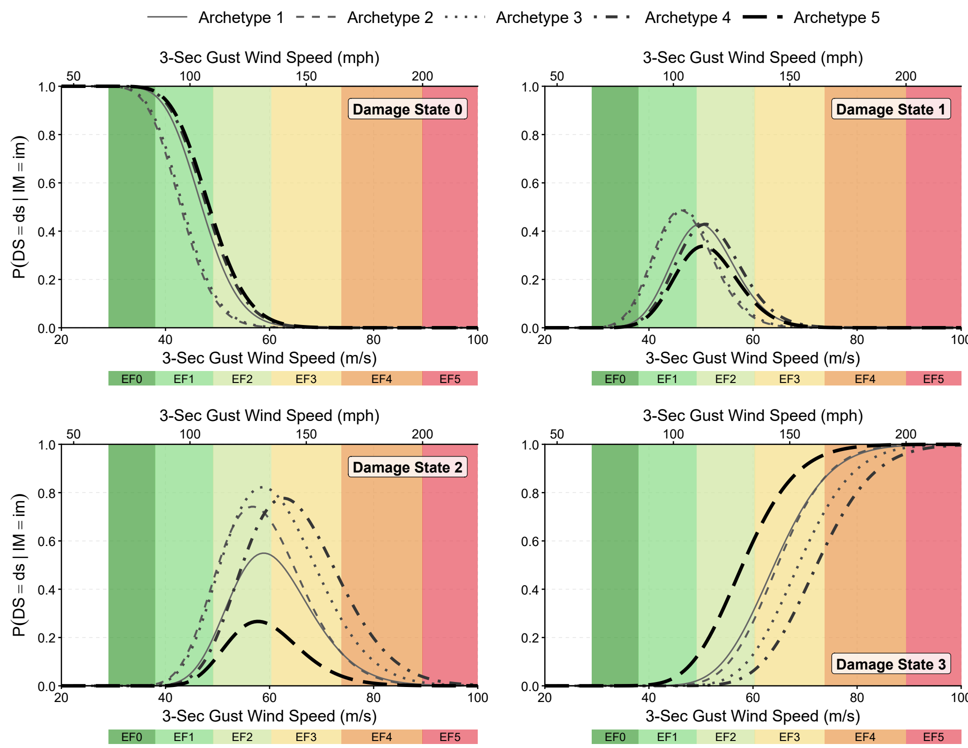

Fig. 22. Probability of building being in a specific DS for the five residential archetypes in Fig. 21.

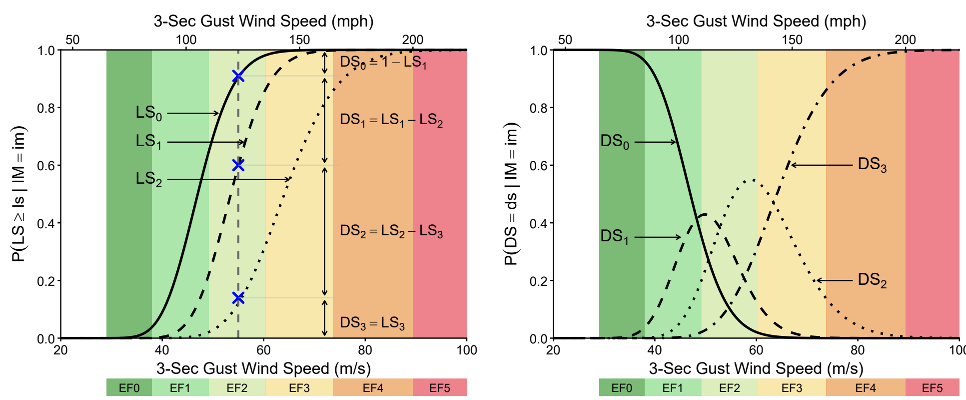

Fig. 23. Relationship between LS (left) and DS (right) for Archetype 1. LS curves are transformed to DS curves according to Eq. 6 and a building being a particular damage state is estimated according to Eq. 7.

APPENDIX III. SENSITIVITY ANALYSIS: AGREEMENT TABLE

The agreement matrices for all DL_1 buildings indicate an overestimation of damage states; however, the model prediction shifts toward underestimation when transitioning to DL_2 and DL_3. Given that higher DLs correspond to increased structural resistance to wind loads, these results suggest that the optimal DL for accurate damage state prediction lies between DL_1 and DL_2—the point at which the transition from overestimation to underestimation occurs.

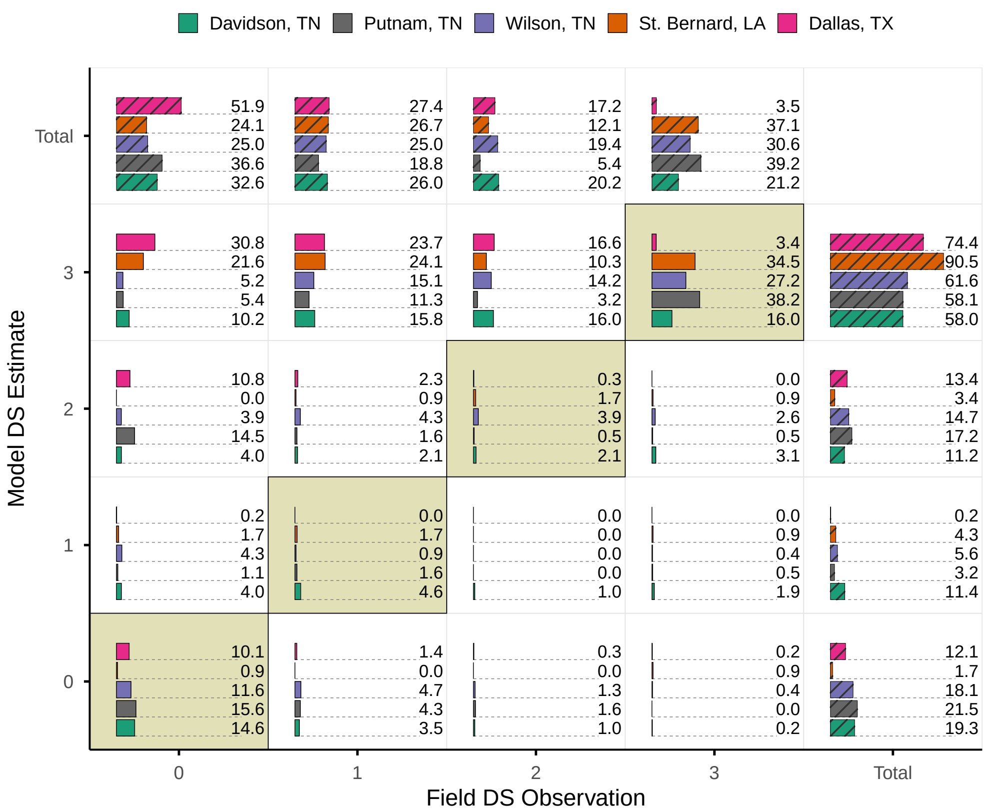

Fig. 24. A percent agreement table showing field-observed and model-estimated classification across four DS classes for the case study areas where DL_1 is assigned to all the buildings.

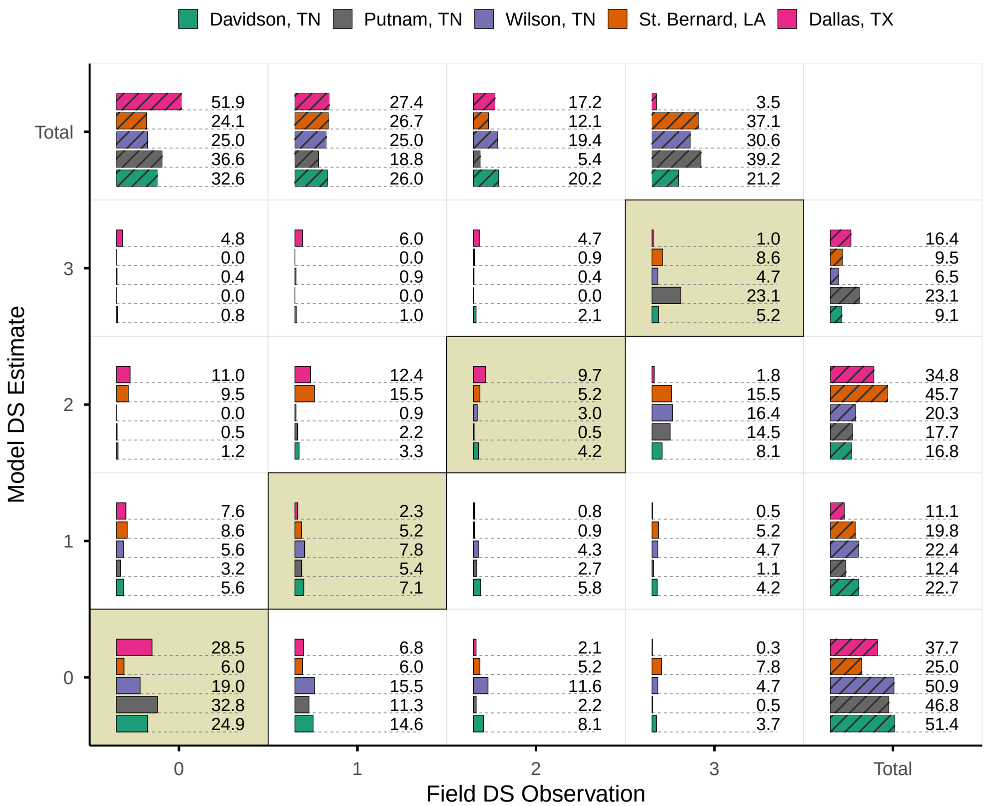

Fig. 25. A percent agreement table showing field-observed and model-estimated classification across four DS classes for the case study areas where DL_2 is assigned to all the buildings.

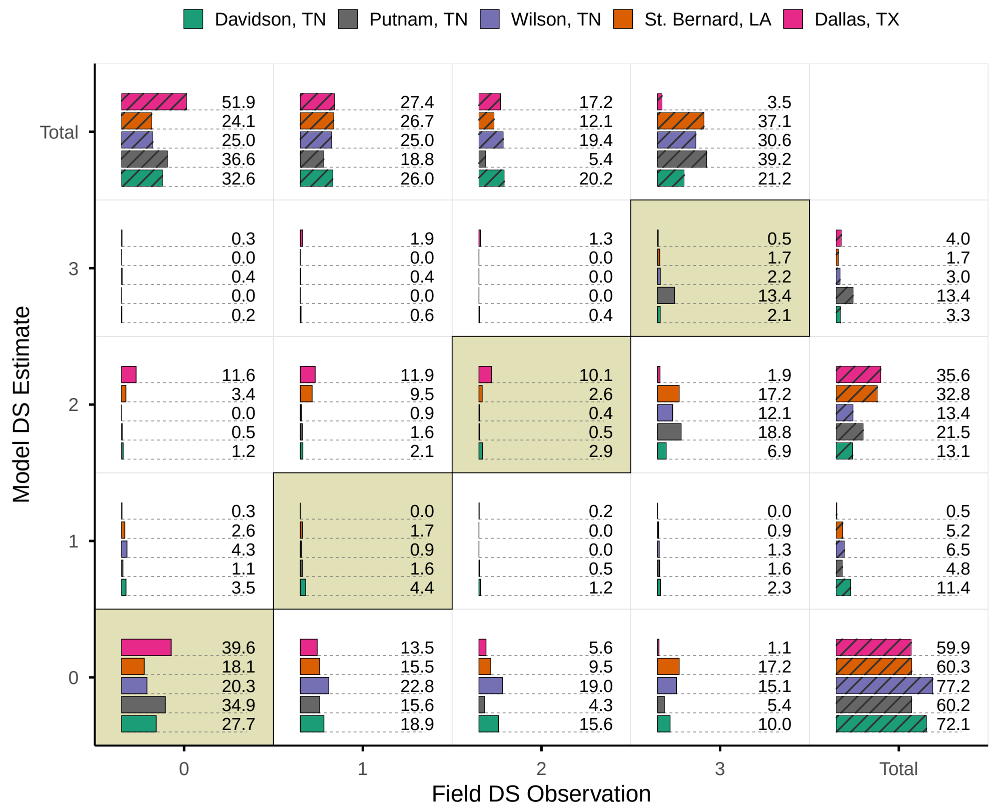

Fig. 26. A percent agreement table showing field-observed and model-estimated classification across four DS classes for the case study areas where DL_3 is assigned to all the buildings.

REFERENCES

Adhikari, P., Mahmoud, H. N., and Ellingwood, B. R. (2021). "Life-cycle cost and sustainability analysis of light-frame wood residential communities exposed to tornados." *Nat. Hazards*, 109(1), 523–544.

Aghababaei, M., Koliou, M., Pilkington, S., Mahmoud, H., van de Lindt, J. W., Curtis, A., Smith, S., Ajayakumar, J., and Watson, M. (2020a). "Validation of Time-Dependent Repair Recovery of the Building Stock Following the 2011 Joplin Tornado." *Nat. Hazard. Rev.*, 21(4), 04020038.

Aghababaei, M., Koliou, M., Pilkington, S., Mahmoud, H., van de Lindt, J. W., Curtis, A., Smith, S., Ajayakumar, J., and Watson, M. (2020b). "Validation of time-dependent repair recovery of the building stock following the 2011 joplin tornado." *Natural Hazards Review*, 21(4), 04020038.

Attary, N., van de Lindt, J. W., Mahmoud, H., Smith, S., Navarro, C. M., Kim, Y. W., and Lee, J. S. (2018). "Hindcasting community-level building damage for the 2011 Joplin EF5 tornado." *Nat. Hazards*, 93(3), 1295–1316.

Bai, J.-W., Hueste, M. B. D., and Gardoni, P. (2013). "Case study: Scenario-based seismic loss estimation for concrete buildings in mid-america." *Earthquake Spectra*, 29(4), 1109–1130.

Brown, T. M. (2010). "Development of a statistical relationship between ground-based and remotely-sensed damage in windstorms." Ph.d. dissertation, Texas Tech University, Lubbock, TX, USA, <http://hdl.handle.net/2346/45185>. Unrestricted availability.

Chen, Z., Wagner, M., Das, J., Doe, R. K., and Cerveny, R. S. (2021). "Data-Driven Approaches for Tornado Damage Estimation with Unpiloted Aerial Systems." *Remote Sens.*, 13(9), 1669.

Cimellaro, G. P., Reinhorn, A. M., and Bruneau, M. (2010). "Framework for analytical quantification of disaster resilience." *Engineering Structures*, 32(11), 3639–3649.

Cimellaro, G. P., Renschler, C., Reinhorn, A. M., and Arendt, L. (2016). "PEOPLES: A framework for evaluating resilience." *Journal of Structural Engineering*, 142(10), 04016063.

Cremen, G. and Baker, J. W. (2019). "Improving FEMA P-58 non-structural component fragility functions and loss predictions." *Bull. Earthquake Eng.*, 17(4), 1941–1960.

Crowley, H., Pinho, R., and Bommer, J. J. (2004). "A probabilistic displacement-based vulnerability assessment procedure for earthquake loss estimation." *Bulletin of Earthquake Engineering*, 2(2), 173–219.

Ellingwood, B. R., Cutler, H., Gardoni, P., Peacock, W. G., van de Lindt, J. W., and Wang, N. (2016). "The centerville virtual community: a fully integrated decision model of interacting physical and social infrastructure systems." *Sustainable and Resilient Infrastructure*, 1(3-4), 95–107.

Ellingwood, B. R., Rosowsky, D. V., Li, Y., and Kim, J. H. (2004). "Fragility Assessment of Light-Frame Wood Construction Subjected to Wind and Earthquake Hazards." *J. Struct. Eng.*, 130(12), 1921–1930.

FEMA (2022). "Hazus hurricane model technical manual hazus 5.1. [Online; accessed 25. Jun. 2024] https://www.fema.gov/sites/default/files/documents/fema_hazus-hurricane-model-technical-manual-5-1.pdf.

Gardoni, P. (2018). *Routledge Handbook of Sustainable and Resilient Infrastructure*. Routledge, New York, NY, USA.

Ghasemi, S., Roohi, M., Sanderson, D., Sediek, O., and van de Lindt, J. W. (2026). "Integrated data imputation of national inventories for bridging information gaps and outcome risk uncertainty in community resilience modeling." *International Journal of Disaster Risk Reduction*, 106077.

Gidaris, I., Padgett, J. E., Barbosa, A. R., Chen, S., Cox, D., Webb, B., and Cerato, A. (2017). "Multiple-hazard fragility and restoration models of highway bridges for regional risk and resilience assessment in the united states: State-of-the-art review." *Journal of Structural Engineering*, 143(3), 04016188.

Graettinger, A. J., Grau, D., Van De Lindt, J., and Prevatt, D. O. (2012). "GIS for the Geo-Referenced Analysis and Rapid Dissemination of Forensic Evidence Collected in the Aftermath of the Tuscaloosa Tornado." *Proceedings*, 2170–2179.

Hill, C. and Levitan, M. (2005). "Development of vulnerability functions for industrial/petrochemical facilities due to extreme winds and hurricanes." *Solutions to Coastal Disasters 2005*, American Society of Civil Engineers, 565–575.

IN-CORE (2024a). "IN-CORE (June). [Online; accessed 18. Jun. 2024] https://github.com/

IN-CORE.

IN-CORE (2024b). "IN-CORE (June). [Online; accessed 18. Jun. 2024] https://incore.ncsa.illinois.edu.

Kalakonas, P., Silva, V., Mouyiannou, A., and Rao, A. (2020). "Exploring the impact of epistemic uncertainty on a regional probabilistic seismic risk assessment model." *Natural Hazards*, 104(1), 997–1020.

Kameshwar, S. and Padgett, J. E. (2014). "Multi-hazard risk assessment of highway bridges subjected to earthquake and hurricane hazards." *Engineering Structures*, 78, 154–166.

Kijewski-Correa, T., Roueche, D. B., Mosalam, K. M., Prevatt, D. O., and Robertson, I. (2021). "StEER: A Community-Centered Approach to Assessing the Performance of the Built Environment after Natural Hazard Events." *Front. Built Environ.*, 7, 636197.

Kuligowski, E., Lombardo, F., Phan, L., Levitan, M., and Jorgensen, D. (2014). "Final report, national institute of standards and technology (nist) technical investigation of the may 22, 2011, tornado in joplin, missouri, <https://tsapps.nist.gov/publication/get_pdf.cfm?pub_id=915628> (2014-03-26 00:03:00).

Landis, J. R. and Koch, G. G. (1977). "The measurement of observer agreement for categorical data." *biometrics*, 159–174.

Lombardo, F. T., Roueche, D. B., and Prevatt, D. O. (2015). "Comparison of two methods of near-surface wind speed estimation in the 22 may, 2011 joplin, missouri tornado." *Journal of Wind Engineering and Industrial Aerodynamics*, 138, 87–97.

Maas, M., Supinie, T., Berrington, A., Emmerson, S., Aidala, A., and Gavan, M. (2024). "The tornado archive: Compiling and visualizing a worldwide, digitized tornado database." *Bulletin of the American Meteorological Society*, 105(7), E1137 – E1152.

Masoomi, H. and van de Lindt, J. W. (2017). "Tornado community-level spatial damage prediction including pressure deficit modeling." *Sustainable and Resilient Infrastructure*.

McAllister, T. (2018). "State of the research in community resilience: progress and challenges." *Sustainable and Resilient Infrastructure*.

McDonald, J. R. and Mehta, K. C. (2006). *A recommendation for an Enhanced Fujita scale (EF-Scale)*. Wind Science and Engineering Center, Texas Tech University.

Memari, M., Attary, N., Masoomi, H., Mahmoud, H., van de Lindt, J. W., Pilkington, S. F., and Ameri, M. R. (2018). "Minimal Building Fragility Portfolio for Damage Assessment of Communities Subjected to Tornadoes." *J. Struct. Eng.*, 144(7), 04018072.

Merhi, A., Brown-Giammanco, T. M., Roueche, D. B., Wood, R. L., Murphy, T. A., Standohar-Alfano, C. D., Childress, O., Stetzer, T., Godfrey, E. S., Godfrey, C. M., and Souhrada, A. J. (2026). "Damage assessment of the 2020 monroe, louisiana, tornado using different remote-sensing methods and enhanced fujita scales." *Natural Hazards Review*, 27(1), 04025062.

Myint, S. W., Yuan, M., Cerveny, R. S., and Giri, C. P. (2008). "Comparison of Remote Sensing Image Processing Techniques to Identify Tornado Damage Areas from Landsat TM Data." *Sensors (Basel, Switzerland)*, 8(2), 1128.

Nasimi, M. and Wood, R. L. (2024). "Using Deep Learning and Advanced Image Processing for the Automated Estimation of Tornado-Induced Treefall." *Remote Sens.*, 16(7), 1130.

NCEI (2024). "Storm Events Database - Search Results | National Centers for Environmental Information (June). [Online; accessed 20. Jun. 2024] https://www.ncdc.noaa.gov/stormevents/.

NCEI (2025). "Annual 2024 Tornadoes Report | National Centers for Environmental Information (NCEI) (January). [Online; accessed 17. Jan. 2025] https://www.ncei.noaa.gov/access/monitoring/monthly-report/tornadoes/202413.

Nevill, J. B. and Lombardo, F. T. (2021). "Empirical tornado resilience model for light-framed wood residential buildings." *Eng. Struct.*, 231, 111840.

NOAA (2020). "12/26/15 North TX Tornado Outbreak." *NOAA's National Weather Service*.

NOAA (2024). "2023: A historic year of U.S. billion-dollar weather and climate disasters." *NOAA Climate* (May). [Online; accessed 18. Jun. 2024] https://www.climate.gov/news-features/blogs/beyond-data/2023-historic-year-us-billion-dollar-weather-and-climate-disasters.

Nofal, O. M., van de Lindt, J. W., Do, T. Q., Yan, G., Hamideh, S., Cox, D. T., and Dietrich, J. C. (2021). “Methodology for regional multihazard hurricane damage and risk assessment.” *Journal of Structural Engineering*, 147(11), 04021128.

NSI (2022). “National Structure Inventory (September). [Online; accessed 18. Jun. 2024] https://nsi.sec.usace.army.mil/downloads.

Padgett, J. E. and DesRoches, R. (2007). “Sensitivity of seismic response and fragility to parameter uncertainty.” *Journal of Structural Engineering*, 133(12), 1710–1718.

Pilkington, S. F., Curtis, A., Mahmoud, H., van de Lindt, J., Smith, S., and Ajayakumar, J. (2021). “Preliminary Documented Recovery Patterns and Observations from Video Cataloged Data of the 2011 Joplin, Missouri, Tornado.” *Nat. Hazard. Rev.*, 22(1), 05020015.

Pita, G., Pinelli, J.-P., Gurley, K., and Mitrani-Reiser, J. (2015). “State of the art of hurricane vulnerability estimation methods: A review.” *Natural Hazards Review*, 16(2), 04014022.

Porter, K., Hamburger, R., and Kennedy, R. (2007). “Practical development and application of fragility functions.” *Structural Engineering Research Frontiers*, American Society of Civil Engineers, 1–16.

Roohi, M., Ghasemi, S., Sediek, O., Jeon, H., van de Lindt, J. W., Shields, M., Hamideh, S., and Cutler, H. (2024). “Multi-disciplinary seismic resilience modeling for developing mitigation policies and recovery planning.” *Resilient Cities and Structures*, 3(2), 66–84.

Roohi, M., van de Lindt, J. W., Rosenheim, N., Hu, Y., and Cutler, H. (2020). “Implication of building inventory accuracy on physical and socio-economic resilience metrics for informed decision-making in natural hazards.” *Structure and infrastructure engineering*, 17(4), 534–554.

Rosowsky, D. V. and Ellingwood, B. R. (2002). “Performance-Based Engineering of Wood Frame Housing: Fragility Analysis Methodology.” *J. Struct. Eng.*, 128(1), 32–38.

Rossetto, T., D’Ayala, D., Ioannou, I., and Meslem, A. (2013). “Evaluation of existing fragility curves.” *SYNER-G: Typology Definition and Fragility Functions for Physical Elements at Seismic Risk*, Geotechnical, Geological and Earthquake Engineering, Springer Netherlands, Dordrecht, 47–93.

Roueche, D., Ambrose, K., Kijewski-Correa, T., Micheli, L., Rawajfih, H., Rihner, M., Prevatt, D., and Robertson, I. (2024a). “Preliminary virtual reconnaissance report (pvrr).” *Report no.*, <https://www.designsafe-ci.org/data/browser/public/designsafe.storage.published/PRJ-2723/#detail-6320497445180215786-242ac116-0001-012>.

Roueche, D., Bagheri Jeddi, A., Do, T., Prevatt, D., and Alam, M. (2023). “Texas and louisiana march 2022 tornado outbreak event briefing, <https://www.designsafe-ci.org/data/browser/public/designsafe.storage.published/PRJ-3443/#details-3038260412014784020-242ac118-0001-012>.

Roueche, D. B., Lombardo, F. T., and Prevatt, D. O. (2017). “Empirical Approach to Evaluating the Tornado Fragility of Residential Structures.” *J. Struct. Eng.*, 143(9), 04017123.

Roueche, D. B., Nakayama, J. O., Kijewski-Correa, T., and Prevatt, D. O. (2024b). “A unified multievent windstorm performance testbed for single-family residential buildings.” *Natural Hazards Review*, 25(2), 04023060.

Roueche, D. B., Nakayama, J. O., Kijewski-Correa, T., and Prevatt, D. O. (2024c). “A unified multievent windstorm performance testbed for single-family residential buildings.” *Natural Hazards Review*, 25(2), 04023060.

Roueche, D. B., Prevatt, D. O., and Lombardo, F. T. (2018). “Epistemic Uncertainties in Fragility Functions Derived from Post-Disaster Damage Assessments.” *ASCE-ASME Journal of Risk and Uncertainty in Engineering Systems, Part A: Civil Engineering*, 4(2), 04018015.

Saeednejad, N. and Padgett, J. E. (2026). “Bridging data gaps in structural fragility modeling through transfer learning: Methodology and case studies.

Schneider, P. J. and Schauer, B. A. (2006). “HAZUS—its development and its future.” *Natural Hazards Review*, 7(2), 40–44.

Silva, V., Akkar, S., Baker, J., Bazzurro, P., Castro, J. M., Crowley, H., Dolsek, M., Galasso, C., et al. (2019). “Current challenges and future trends in analytical fragility and vulnerability modeling.” *Earthquake Spectra*, 35(4), 1927–1952.

Standohar-Alfano, C. D. and van de Lindt, J. W. (2015). “Empirically Based Probabilistic Tornado Hazard Analysis of the United States Using 1973–2011 Data." *Nat. Hazard. Rev.*, 16(1), 04014013.

Vanbelle, S. (2016). "A new interpretation of the weighted kappa coefficients." *Psychometrika*, 81(2), 399–410.

Vickery, P. J., Skerlj, P. F., Lin, J., Twisdale, L. A., Young, M. A., and Lavelle, F. M. (2006a). "HAZUS-MH hurricane model methodology. ii: Damage and loss estimation." *Natural Hazards Review*, 7(2), 94–103.

Vickery, P. J., Skerlj, P. F., Lin, J., Twisdale, L. A., Young, M. A., and Lavelle, F. M. (2006b). "Hazus-mh hurricane model methodology. ii: Damage and loss estimation." *Natural Hazards Review*, 7(2), 94–103.

Wakimoto, R. M., Atkins, N. T., and Wurman, J. (2011). "The lagrange tornado during vortex2. part i: Photogrammetric analysis of the tornado combined with single-doppler radar data." *Monthly Weather Review*, 139(7), 2233 – 2258.

Wang, W. L. and van de Lindt, J. W. (2021a). "Quantitative modeling of residential building disaster recovery and effects of pre- and post-event policies." *Int. J. Disaster Risk Reduct.*, 59, 102259.

Wang, W. L. and van de Lindt, J. W. (2021b). "Quantitative modeling of residential building disaster recovery and effects of pre-and post-event policies." *International Journal of Disaster Risk Reduction*, 59, 102259.

Wang, W. L. and van de Lindt, J. W. (2022). "Quantifying the effect of improved school and residential building codes for tornadoes in community resilience." *Resilient Cities and Structures*, 1(1), 65–79.

Wang, W. T. L., van de Lindt, J. W., Cutler, H., Rosenheim, N., Koliou, M., Lee, J. S., and Calderon, D. (2021). "Community resilience assessment of an EF-5 tornado using the IN-CORE modeling environment." *Life-Cycle Civil Engineering: Innovation, Theory and Practice*, CRC Press, Boca Raton, FL, USA, 394–398.

Wood, R. L., Roueche, D., Cullum, K., Davis, B., Gutierrez Soto, M., Javadinasab Hormozabad, S., Liao, Y., Lombardo, F., Moravej, M., Pilkington, S., Prevatt, D., Kijewski-Correa, T., DJIMA, W., and Robertson, I. (2024). "Early access reconnaissance report (earr)." *Report no.*, <https://www.designsafe-ci.org/data/browser/public/designsafe.storage.published/PRJ-2723/#detail-2377181520534629910-242ac116-0001-012>.